Volume 11
Number 36
28 September 2020
Pages 9717–10006

Chemical Science

rsc.li/chemical-science

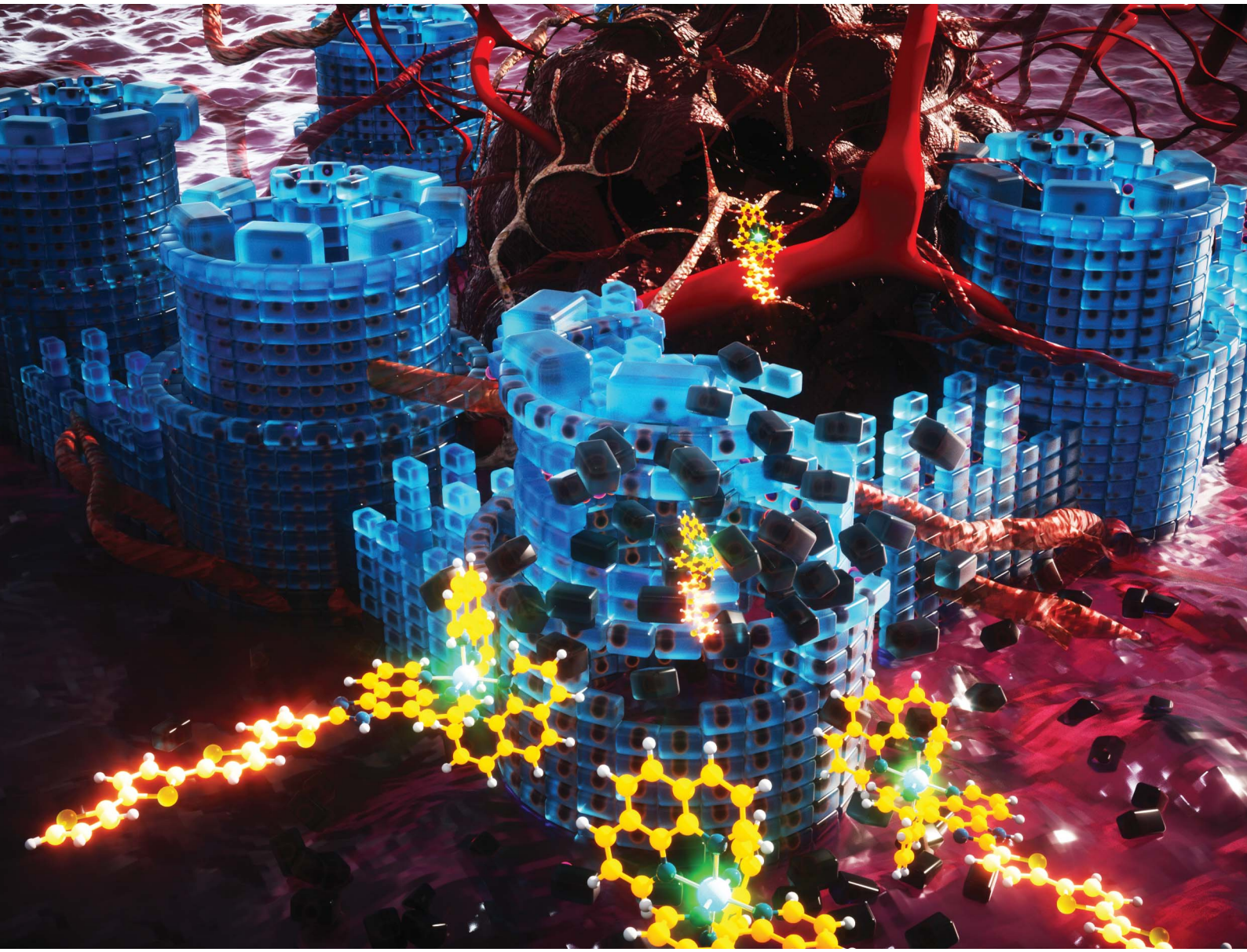

ISSN 2041-6539

ROYAL SOCIETY OF CHEMISTRY

EDGE ARTICLE

Colin G. Cameron, Marta E. Alberto, Sherri A. McFarland *et al.*
Breaking the barrier: an osmium photosensitizer with unprecedented hypoxic phototoxicity for real world photodynamic therapy

Chemical Science

ROYAL SOCIETY OF CHEMISTRY

EDGE ARTICLE

View Article Online
View Journal | View Issue

Cite this: *Chem. Sci.*, 2020, **11**, 9784

All publication charges for this article have been paid for by the Royal Society of Chemistry

Breaking the barrier: an osmium photosensitizer with unprecedented hypoxic phototoxicity for real world photodynamic therapy†

John A. Roque III, [ab] Patrick C. Barrett,‡[a] Houston D. Cole, [b] Liubov M. Lifshits, [b] Ge Shi,§[c] Susan Monro,[c] David von Dohlen,[a] Susy Kim,[d] Nino Russo, [e] Gagan Deep,[d] Colin G. Cameron, *[ab] Marta E. Alberto *[e] and Sherri A. McFarland *[abc]

Hypoxia presents a two-fold challenge in the treatment of cancer, as low oxygen conditions induce biological changes that make malignant tissues simultaneously more aggressive and less susceptible to standard chemotherapy. This paper reports the first metal-based photosensitizer that approaches the ideal properties for a phototherapy agent. The Os(phen)$_2$-based scaffold was combined with a series of IP-*n*T ligands, where phen = 1,10-phenanthroline and IP-*n*T = imidazo[4,5-*f*][1,10]phenanthroline tethered to *n* = 0–4 thiophene rings. **Os-4T** (*n* = 4) emerged as the most promising complex in the series, with picomolar activity and a phototherapeutic index (PI) exceeding 10^6 in normoxia. The photosensitizer exhibited an unprecedented PI > 90 (EC_{50} = 0.651 μM) in hypoxia (1% O_2) with visible and green light, and a PI > 70 with red light. **Os-4T** was also active with 733 nm near-infrared light (EC_{50} = 0.803 μM, PI = 77) under normoxia. Both computation and spectroscopic studies confirmed a switch in the nature of the lowest-lying triplet excited state from triplet metal-to-ligand charge transfer (^{3}MLCT) to intraligand charge transfer (^{3}ILCT) at *n* = 3, with a lower energy and longer lifetime for *n* = 4. All compounds in the series were relatively nontoxic in the dark but became increasingly phototoxic with additional thiophenes. These normoxic and hypoxic activities are the largest reported to date, demonstrating the utility of osmium for phototherapy applications. Moreover, **Os-4T** had a maximum tolerated dose (MTD) in mice that was >200 mg kg^{-1}, which positions this photosensitizer as an excellent candidate for *in vivo* applications.

Received 28th May 2020
Accepted 3rd August 2020

DOI: 10.1039/d0sc03008b

rsc.li/chemical-science

1. Introduction

Cancer remains a leading cause of death in many countries.[1] There are ongoing efforts to develop adjuvant or alternative approaches that complement conventional treatment modalities, *e.g.*, surgery, radiotherapy, chemotherapy, and more recently immunotherapy.[2–4] A persistent challenge has been resistance, either intrinsic or acquired, which causes subpopulations of cancerous cells to evade treatment and potentially metastasize.[5–7] There are multiple mechanisms for resistance, but specific physiological conditions, particularly hypoxia, are known to drive the mutator phenotype, and increase the ability for cancer cells to survive and persist despite the utilization of different therapeutic approaches.[7–10]

Light-based therapies, such as photodynamic therapy (PDT) and the relatively new field of photochemotherapy (PCT), are examples of locally administered treatments where light-responsive prodrugs are used to selectively target tumors while sparing healthy tissue. PDT, which has been known for over a hundred years and is clinically approved,[11–23] employs an otherwise nontoxic photosensitizer (PS) that can be activated by therapeutic wavelengths of light to form cytotoxic singlet oxygen ($^1O_2$) and other reactive oxygen species (ROS). Due to this oxygen dependence, PDT can be less effective in treating hypoxic tumors. However, the very fact that ROS do not rely on a single biological mechanism of action (in contrast to kinase

[a]*Department of Chemistry and Biochemistry, The University of North Carolina at Greensboro, Greensboro, North Carolina, 27402 USA*

[b]*Department of Chemistry and Biochemistry, The University of Texas at Arlington, Arlington, Texas, 76019 USA. E-mail: colin.cameron@uta.edu; sherri.mcfarland@uta.edu*

[c]*Department of Chemistry, Acadia University, Wolfville, Nova Scotia, B4P 2R6 Canada*

[d]*Department of Cancer Biology, Wake Forest School of Medicine, Winston Salem, NC, 27157, USA*

[e]*Dipartimento di Chimica e Tecnologie Chimiche, Università della Calabria, Arcavacata di Rende, 87036 Italy. E-mail: marta.alberto@unical.it*

† Electronic supplementary information (ESI) available: Supplemental methodology, synthetic characterization (1D and 2D NMR, HPLC, HRMS), spectroscopic characterization (emission, TA), computational predictions (ground and excited states), (photo)biological evaluations, and the various acronyms used in-text. See DOI: 10.1039/d0sc03008b

‡ Present address: Carilion School of Medicine, Virginia Polytechnic Institute and State University, Roanoke, Virginia, 24016, USA.

§ Present address: Department of Pathology, Dalhousie University, Halifax, Nova Scotia, B3H 4R2 Canada.

inhibitors, for example) makes it more difficult for cells to achieve resistance to PDT.[24] This motivates new approaches to circumvent the limitations of low oxygen tension.

Alternatively, PCT has been proposed as a strategy that exploits oxygen-independent reaction pathways (*e.g.*, photocaging or photocisplatin agents) with the potential advantage of maintaining activity toward hypoxic malignancies. Ru(II)-based metal complexes have emerged as PCT agents with modular architectures that can be tuned to be relatively inert in the absence of light, to photodecompose *via* ligand loss with visible light in the absence of oxygen, and to be less susceptible than other metallodrugs like cisplatin[25] to deactivation by cellular thiols.[26–41] Many of these Ru(II) coordination complexes are relatively simple to synthesize in high purity, exhibit aqueous solubility as their chloride salts, and have photophysical properties that can be tuned by rational design according to the well-developed principles from the Ru(II) polypyridyl literature.[23,42–47]

In contrast to PDT, PCT agents rely on engaging a specific cellular target or utilizing a specific mechanism of action, which cancer cells may already be able to evade, particularly under hypoxic conditions. In addition to the potential issues associated with utilizing specific mechanisms of action, PCT agents possess some technical limitations. Phototriggered ligand dissociation is a stoichiometric process that would require higher dosing than a catalytic drug to achieve efficacy. In addition, a mixture of potentially new (and difficult to identify) decomposition products are produced *in situ*. The impact of a hypoxic environment (with different pH, potential quenching mechanisms, and protein expression levels) on the photochemical process is challenging to ascertain.

Indeed, a careful review of the literature reveals that very few systems – that are believed to be active under hypoxia – have actually been tested against cells under low oxygen conditions.[41,48–54] Likewise, relatively few systems have been tested for photodissociation in cell-free conditions under low oxygen conditions (*i.e.*, 0–3%).[37,49,50,52,55] Performing experiments under hypoxic conditions is challenging due to a variety of factors such as the initial establishment of low oxygen tension or differences in cellular growth and metabolism – if the cells can even grow at the desired oxygen level. A hypoxia chamber for cell incubation and processing is required to establish and maintain a low oxygen atmosphere, but many light devices do not fit inside the chamber and/or result in excessive heating in the chamber. Maintaining a low oxygen atmosphere during the time of irradiation outside the chamber is challenging but critical since the PCT agents are designed to release their phototoxic payloads immediately upon light exposure. We have applied qPCR (high transparency) films over well plates for this purpose (up to 384 wells). While not perfectly gas impermeable, they do mitigate gas exchange over the period of the light treatment ($\sim$20 °C, $\leq$1.5 h). Interassay reproducibility (in terms of maintaining hypoxia during illumination) is excellent so long as oxygen-sensitive controls for leaky films or poor gas exchange are included.

We are committed to developing hypoxia active metal complexes and have established a protocol for effective testing. Using this rigorous experimental design for evaluation, we developed one compound with Glazer's group, [Ru(6,6′-dmb)$_2$(1-NIP)]Cl$_2$, that exhibited the largest known hypoxia phototherapeutic index (PI) at the time of its publication (PI = 15 at 1% O_2). This is marginal compared to good normoxic values for PDT agents (PI > 1000), and unfortunately, it did not work with red light (630 nm), the clinically approved wavelength for PDT.[41] Similar PIs for PCT agents that release cytotoxic ligands and/or metal complexes have been reported.[27,29,50,56]

These findings inspired us to consider other ways of instilling hypoxic activity in Ru(II) complexes that are photostable and exploit photocatalytic pathways/mechanisms for cytotoxic effects. Our approach is to create metal complex PSs that combine powerful $^1O_2$ sensitization, such that some activity can be maintained even in hypoxia, with the possibility of light-induced electron transfer reactions *via* triplet intraligand charge transfer (^{3}ILCT) excited states. Our own TLD1433, now in phase II human clinical trials (NCT03945162) for treating bladder cancer with PDT, was born out of this work.[23]

In the present study we demonstrate the feasibility of this approach using Os(II) as the metal combined with the same class of oligothienyl-appended ligands that feature in TLD1433.[23,57] The Os(II) complexes provide longer wavelength absorption windows compared to their Ru(II) analogues, due to the more pronounced heavy atom effect.[58] Larger spin–orbit coupling (SOC) associated with the Os(II) center also leads to faster intersystem crossing (ISC), producing triplet states in high yield.[59,60] The prolonged excited state lifetimes characteristic of ^{3}ILCT states result in sensitivity to trace oxygen.[61] Finally, we have previously shown that certain Os(II) complexes are tolerated *in vivo*, can be panchromatically activated with visible and near-infrared (NIR) wavelengths of light, and give rise to phototoxic effects both *in vitro* and *in vivo*.[62,63]

Here we introduce an Os(II)-based PS (**Os-4T**) that is extremely potent, can be activated with NIR light (733 nm), and exhibits photocytotoxic effects in hypoxia (1% O_2). To our knowledge, this complex is the first hypoxia-active Os(II)-based PS and it exhibits one of the largest PIs that we have encountered to date. This PS was part of a systematic study of a family of related [Os(phen)$_2$(IP-*n*T)]Cl$_2$ complexes, where phen = 1,10-phenanthroline, IP = imidazo[4,5-*f*][1,10]phenanthroline, and *n*T = thiophenes of varying chain lengths *n* (*n* = 0–4) (Chart 1). This allowed for a rigorous investigation of the effects of *n* on

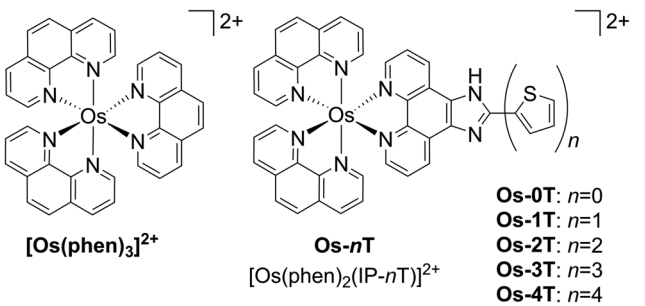

Chart 1 Molecular structures of reference compound [Os(phen)$_3$]$^{2+}$ and **Os-0T**–**Os-4T**. The chloride salts were used unless otherwise specified. The compounds were racemic mixtures of the Δ/Λ isomers.

computed ground and excited state properties, time-resolved photophysics, and photobiology. In this report, we discuss these studies and provide a rationale for the observed photobiology, along with a road map for the theory-driven design of next-generation agents.

2. Materials and methods

2.1 Materials

Unless otherwise specified, all reagents and solvents were purchased from commercial sources and used without further purification. Water used for all biological experiments was deionized to a resistivity $\geq$ 18.2 MΩ using either a Barnstead or Milli-Q® filtration system. Saturated solvents for log *D* experiments were prepared in-house using 10 mM phosphate buffer solution (saline-free PBS) and 1-octanol (99.9%). Buffers were checked for an accurate pH against a two-point calibrated VWR® B10P pH meter ($pH_{ref.}$ = 4.00, 7.00; Fisher Science Education, S25849A/B).

2.2 Instrumentation

Microwave reactions were performed in a CEM Discover microwave reactor. Flash chromatography relied on the Teledyne Isco CombiFlash® EZ Prep system with Silicycle SiliaSep silica flash cartridges (FLH-R10030B-ISO25). Size-exclusion chromatography was performed on a gravity column packed with Sephadex® LH-20. NMR spectra were collected using a JEOL ECA 500 NMR spectrometer (^{1}H, ^{1}H–^{1}H COSY) at the NMR facility at the University of North Carolina at Greensboro (UNCG) and Agilent 700 MHz NMR spectrometer (^{13}C, ^{13}C–^{1}H HSQC, ^{13}C–^{1}H HMBC) at the Joint School of Nanoscience and Nanoengineering at Greensboro (JSNN). The chemical shifts are reported in parts per million (ppm) and were referenced to the residual solvent peaks. ESI mass spectra were obtained using a Thermo Fisher LTQ Orbitrap XL coupled to a Water's Acquity Ultra Performance Liquid Chromatography (UPLC) stack using a BEH C18 column at UNCG's Triad Mass Spectrometry facility. HPLC analyses were carried out on an Agilent/Hewlett Packard 1100 series instrument (ChemStation Rev. A. 10.02 software) using a Hypersil GOLD C18 column (Thermo 25005-254630, guard 25003-014001) with an A–B gradient (40 min run; 98% → 5% A; A = 0.1% formic acid in water, B = 0.1% formic acid in acetonitrile (MeCN)). Reported retention times are accurate to within ±0.1 min.

2.3 Synthesis

The $Os(phen)_2Cl_2$ intermediate[58] and imidazo[4,5-*f*][1,10]phenanthroline (IP) based ligands[64] were prepared according to adapted literature procedures. The synthesis of IP-based ligands follows the synthesis of IP-4T that is described below. [2,2′:5′,2″:5″,2‴-Quaterthiophene]-5-carbaldehyde (4T-CHO) was prepared as previously described[65] *via* the coupling of 5-bromo-5″-formyl-2,2′:5′,2″-terthiophene with 2-(tributylstannyl) thiophene, which were purchased from Alfa Aesar and Fisher Scientific, respectively.

Complexes **Os-0T–Os-4T** have not previously been reported and were isolated as their PF_6^- salts. Cl^- salts were obtained from corresponding PF_6^- salts *via* anion metathesis on HCl-treated Amberlite IRA-410 resin (Alfa-Aesar, A1773436) with methanol as the eluent. Final complexes were a racemic mixture of Δ/Λ isomers. $[Os(phen)_3]^{2+}$ and **Os-0T–Os-4T** were characterized by TLC, ^{1}H NMR and ^{1}H–^{1}H COSY NMR (Fig. S-1–S-6†), high-resolution ESI^+-MS (Fig. S-10–S-15†), and HPLC (Fig. S-16–S-21†). COSY was not collected for $[Os(phen)_3]^{2+}$. NMR assignments were made in consultation with a literature source.[66] Compound **Os-4T** required additional ^{13}C, ^{13}C–^{1}H HSQC, and ^{13}C–^{1}H HMBC NMR data for the full assignment of the ^{1}H NMR signals of the quaterthiophene group (Fig. S-7–S-9†). Biological studies were carried out on Cl^- salts and photophysical measurements were carried out on PF_6^- salts.

2.3.1 IP-4T. 1,10-Phenanthroline-5,6-dione (175 mg, 0.83 mmol), 4T-CHO (200 mg, 0.56 mmol), and ammonium acetate (1.38 g, 18 mmol) were added to a 250 mL round-bottom flask with glacial acetic acid (100 mL). The orange mixture was heated at 100 °C for 96 hours. Once cooled, the reddish-brown mixture was neutralized with NH_4OH. The precipitate was vacuum filtered using a Buchner funnel and washed with cold deionized water (50 mL) and cold ether (100 mL) to obtain the desired product as a brown solid (279 mg, 91%). ^{1}H NMR (500 MHz, DMSO-d_6, ppm): δ 9.05 (dd, J = 4.2, 1.7 Hz, 2H), 8.85 (d, J = 7.9 Hz, 2H), 7.88–7.81 (m, 3H), 7.57 (d, J = 4.7 Hz, 1H), 7.52 (d, J = 3.8 Hz, 1H), 7.48 (d, J = 3.9 Hz, 1H), 7.41–7.36 (m, 3H), 7.32 (d, J = 3.7 Hz, 1H), 7.13 (dd, J = 5.1, 3.5 Hz, 1H).

2.3.2 $[Os(phen)_3]^{2+}$. While this complex may be synthesized following a published procedure,[67] it was isolated in this case as a side-product from synthesis of another compound and confirmed to be pure $[Os(phen)_3]Cl_2$ by ^{1}H NMR, mass spectrometry and HPLC (Fig. S-1, S-10 and S-16†). ^{1}H NMR (500 MHz, MeOD-d_3, ppm): δ 8.48 (d, J = 8.0 Hz, 6H; 4,7), 8.32 (s, 6H; 5,6), 8.03 (d, J = 5.5 Hz, 6H; 2,9), 7.66 (dd, J = 8.0, 5.5 Hz, 6H; 3,8). HRMS (ESI^+) m/z: $[M - 2Cl]^{2+}$ calcd for $C_{36}H_{24}N_6Os$ 366.0833; found 366.0821. HPLC retention time: 9.43 min (97% purity by peak area).

2.3.3 $[Os(phen)_2(IP)]^{2+}$ (Os-0T). $Os(phen)_2Cl_2$ (99 mg, 0.16 mmol) and IP (35 mg, 0.16 mmol) were added to a microwave vessel containing argon-purged ethylene glycol (2.5 mL) and subjected to microwave irradiation at 180 °C for 15 minutes. The resulting black mixture was transferred to a separatory funnel with deionized water (20 mL) and CH_2Cl_2 (30 mL). After gentle mixing, the CH_2Cl_2 was drained and the remaining aqueous layer was washed with CH_2Cl_2 (30 mL portions) until the CH_2Cl_2 was colorless. At that point, another 30 mL of CH_2Cl_2 was added and allowed to settle to the bottom of the separatory funnel. Then, saturated aqueous KPF_6 (5 mL) was added, and the mixture shaken gently and allowed to partition over time to facilitate transfer of the product from the aqueous layer to the CH_2Cl_2 layer, which was collected and concentrated under reduced pressure. The crude product was purified by silica gel flash column chromatography with a gradient of MeCN, 10% water in MeCN, followed by 7.5% water in MeCN with 0.5% KNO_3 to obtain $[Os(phen)_2(IP)](PF_6)_2$ as a black solid (28 mg, 16%). A portion of the PF_6^- salt was converted to its corresponding Cl^- salt $[Os(phen)_2(IP)]Cl_2$ in quantitative yield using Amberlite IRA-410 with MeOH as the eluent. R_f = 0.08

(0.5% KNO_3, 7.5% H_2O, 92% MeCN). ^{1}H NMR (500 MHz, MeOD-d_3, ppm): δ 8.78 (br s, 2H; c), 8.72 (s, 1H; d), 8.48 (d, J = 8.0 Hz, 4H; 4,7), 8.32 (s, 4H; 5,6), 8.06 (d, J = 5.4 Hz, 2H; 2), 8.02 (d, J = 5.4 Hz, 2H; 9), 7.98 (d, J = 5.5 Hz, 2H; a), 7.68 (dd, J = 8.5, 5.5 Hz, 2H; b), 7.67–7.63 (m, 4H; 8,3). HRMS (ESI$^+$) m/z: $[M - 2Cl]^{2+}$ calcd for $C_{37}H_{24}N_8Os$ 386.0864; found 386.0856. $[M - 2Cl - H]^+$ calcd for $C_{37}H_{23}N_8Os$ 771.1655; found 771.1646. HPLC retention time: 9.20 min (100% purity by peak area).

2.3.4 $[Os(phen)_2(IP\text{-}1T)]^{2+}$ (Os-1T). $Os(phen)_2Cl_2 \cdot 2H_2O$ (66 mg, 0.1 mmol) and IP-1T (30.2 mg, 0.1 mmol) were combined and treated according to the procedure described for **Os-0T** to yield $[Os(phen)_2(IP\text{-}1T)](PF_6)_2$ as a black solid (36 mg, 31%). A portion of the PF_6^- salt was converted to its corresponding Cl^- salt $[Os(phen)_2(IP\text{-}1T)]Cl_2$ in quantitative yield using Amberlite IRA-410 with MeOH as the eluent. R_f = 0.17 (0.5% KNO_3, 7.5% H_2O, 92% MeCN). ^{1}H NMR (500 MHz, MeOD-d_3, ppm): δ 8.87 (d, J = 8.1 Hz, 2H; c), 8.48 (d, J = 8.2 Hz, 4H; 4,7), 8.32 (s, 4H; 5,6), 8.09 (d, J = 5.3 Hz, 2H; 2), 8.04 (dd, J = 3.8 Hz, 1.0 Hz, 1H; d), 8.03 (d, J = 5.3 Hz, 2H; 9), 7.98 (d, J = 5.6 Hz, 2H; a), 7.76 (d, J = 5.1 Hz, 1H; f), 7.71–7.63 (m, 6H; b, 3,8), 7.31 (dd, J = 5.1 Hz, 3.9 Hz, 1H; e). HRMS (ESI$^+$) m/z: $[M - 2Cl]^{2+}$ calcd for $C_{41}H_{26}N_8OsS$ 427.0802; found 427.0782. $[M - 2Cl - H]^+$ calcd for $C_{41}H_{25}N_8OsS$ 853.1532; found 853.1505. HPLC retention time: 11.12 min (99% purity by peak area).

2.3.5 $[Os(phen)_2(IP\text{-}2T)]^{2+}$ (Os-2T). $Os(phen)_2Cl_2 \cdot 2H_2O$ (66 mg, 0.1 mmol) and IP-2T (38.4 mg, 0.1 mmol) were combined and treated according to the procedure described for **Os-0T** to yield $[Os(phen)_2(IP\text{-}2T)](PF_6)_2$ as a black solid (39 mg, 32%). The PF_6^- salt was converted to its corresponding Cl^- salt $[Os(phen)_2(IP\text{-}2T)]Cl_2$ in quantitative yield using Amberlite IRA-410 with MeOH as the eluent and further purified using size-exclusion chromatography on Sephadex LH-20 with MeOH as the eluent (32 mg, 88%). R_f = 0.18 (0.5% KNO_3, 7.5% H_2O, 92% MeCN). ^{1}H NMR (500 MHz, MeOD-d_3, ppm): δ 8.62 (d, J = 8.0 Hz, 2H; c), 8.51 (d, J = 8.9 Hz, 2H; 4), 8.49 (d, J = 8.6 Hz, 2H; 7), 8.35 (s, 4H; 5,6), 8.21 (d, J = 5.1 Hz, 2H; 2), 8.04 (d, J = 5.0 Hz, 2H; 9), 7.95 (d, J = 4.7 Hz, 2H; a), 7.90 (d, J = 3.9 Hz, 1H; d), 7.74 (dd, J = 8.5, 5.0 Hz, 2H; 3), 7.68 (dd, J = 8.5, 5.0 Hz, 2H; 8), 7.53 (dd, J = 8.0, 5.0 Hz, 2H; b), 7.32 (d, J = 4.9 Hz, 1H; h), 7.15 (d, J = 3.8 Hz, 1H; e), 7.03 (d, J = 3.1 Hz, 1H; f), 6.97 (dd, J = 5.0, 3.5 Hz, 1H; g). HRMS (ESI$^+$) m/z: $[M - 2Cl]^{2+}$ calcd for $C_{45}H_{28}N_8OsS_2$ 468.0741; found 468.0730. $[M - 2Cl - H]^+$ calcd for $C_{45}H_{27}N_8OsS_2$ 935.1409; found 935.1406. HPLC retention time: 21.28 min (96% purity by peak area).

2.3.6 $[Os(phen)_2(IP\text{-}3T)]^{2+}$ (Os-3T). $Os(phen)_2Cl_2 \cdot 2H_2O$ (66 mg, 0.1 mmol) and IP-3T (47 mg, 0.1 mmol) were combined and treated according to the procedure described for **Os-0T** to yield $[Os(phen)_2(IP\text{-}3T)](PF_6)_2$ as a black solid (35 mg, 27%). The PF_6^- salt was converted to its corresponding Cl^- salt $[Os(phen)_2(IP\text{-}3T)]Cl_2$ in quantitative yield using Amberlite IRA-410 with MeOH as the eluent and further purified using size-exclusion chromatography on Sephadex LH-20 with MeOH as the eluent (23 mg, 81%). R_f = 0.18 (0.5% KNO_3, 7.5% H_2O, 92% MeCN). ^{1}H NMR (500 MHz, MeOD-d_3, ppm): δ 8.77 (d, J = 8.2 Hz, 2H; c), 8.50 (d, J = 8.0 Hz, 2H; 4), 8.48 (d, J = 8.6 Hz, 2H; 7), 8.33 (s, 4H; 5,6), 8.15 (d, J = 5.4 Hz, 2H; 2), 8.03 (d, J = 5.3 Hz, 2H; 9), 7.95 (d, J = 5.3 Hz, 2H; a), 7.89 (d, J = 3.7 Hz, 1H; d), 7.71 (dd, J = 7.8, 5.3 Hz, 2H; 3), 7.66 (dd, J = 8.0, 5.3 Hz, 2H; 8), 7.61 (dd, J = 7.9, 5.3 Hz, 2H; b), 7.34 (d, J = 5.1 Hz, 1H; j), 7.20 (d, J = 3.5 Hz, 2H; e,h), 7.12 (d, J = 3.6 Hz, 1H; f), 7.06 (d, J = 3.5 Hz, 1H; g), 7.04 (dd, J = 4.5, 3.5 Hz, 1H; 1H; i). HRMS (ESI$^+$) m/z: $[M - 2Cl]^{2+}$ calcd for $C_{49}H_{30}N_8OsS_3$ 509.0680; found 509.0664. $[M - 2Cl - H]^+$ calcd for $C_{49}H_{29}N_8OsS_3$ 1017.1287; found 1017.1283. HPLC retention time: 22.81 min (95% purity by peak area).

2.3.7 $[Os(phen)_2(IP\text{-}4T)]^{2+}$ (Os-4T). $Os(phen)_2Cl_2$ (122 mg, 0.2 mmol) and IP-4T (90 mg, 0.16 mmol) were combined and treated according to the procedure described for **Os-0T** to yield $[Os(phen)_2(IP\text{-}4T)](PF_6)_2$ as a black solid (136 mg, 60%). The PF_6^- salt was converted to its corresponding Cl^- salt $[Os(phen)_2(IP\text{-}4T)]Cl_2$ in quantitative yield using Amberlite IRA-410 with MeOH as the eluent and a portion (57 mg) was further purified using size-exclusion chromatography on Sephadex LH-20 with MeOH as the eluent (42 mg, 74%). R_f = 0.28 (0.5% KNO_3, 7.5% H_2O, 92% MeCN). ^{1}H NMR (500 MHz, MeOD-d_3, ppm): δ 8.82 (d, J = 8.3 Hz, 2H; c), 8.49 (d, J = 8.5 Hz, 2H; 4), 8.48 (d, J = 8.0 Hz, 2H; 7), 8.33 (s, 4H; 5,6), 8.12 (d, J = 5.6 Hz, 2H; 2), 8.03 (d, J = 5.3 Hz, 2H; 9), 7.95 (d, J = 5.3 Hz, 2H; a), 7.89 (d, J = 3.8 Hz, 1H; d), 7.69 (dd, J = 8.5, 5.5 Hz, 2H; 3), 7.66 (dd, J = 8.0, 5.5 Hz, 2H; 8), 7.63 (dd, J = 8.5, 5.5 Hz, 2H; b), 7.33 (d, J = 4.0 Hz, 1H; e), 7.29 (dd, J = 5.1, 1.0 Hz, 1H; l), 7.23 (d, J = 3.7 Hz, 1H; f), 7.17 (dd, J = 3.7, 1.0 Hz, 1H; j), 7.12 (d, J = 3.6 Hz, 1H; h), 7.08 (d, J = 3.8 Hz, 1H; g), 7.04 (d, J = 3.9 Hz, 1H; i), 7.00 (dd, J = 5.2, 3.5 Hz, 1H; k). ^{13}C NMR (175 MHz, MeOH-d_3, ppm): δ 153.31 (2), 153.15 (9), 151.38 (21), 151.29 (20), 150.87 (a), 150.42 (10), 149.40 (22,24), 141.39 (12), 138.30 (14), 138.15 (16), 138.06 (4,7), 137.79 (17), 136.39 (15), 136.28 (13), 132.82–132.80 (18,19,23), 132.20 (11), 131.57 (c), 129.67 (5/6), 129.65 (5/6), 129.54 (d), 129.11 (k), 127.50 (3), 127.48 (8), 127.34 (b), 126.82 (f), 126.06 (l), 126.02 (h), 125.87 (e), 125.74 (g), 125.53 (i), 125.08 (j). HRMS (ESI$^+$) m/z: $[M - 2Cl]^{2+}$ calcd for $C_{53}H_{32}N_8OsS_4$ 550.0618; found 550.0601. $[M - 2Cl - H]^+$ calcd for $C_{53}H_{31}N_8OsS_4$ 1099.1164; found 1099.1154. HPLC retention time: 24.14 min (98% purity by peak area).

2.4 Lipophilicity

The relative lipophilicities (or distribution coefficient, D, at pH = 7.4) of the complexes were determined using a modified "shake flask" method as described in previous work.[65] A saturated solution of 1-octanol with water was prepared by mixing 16 mL of 1-octanol (99.9%) with 4 mL of 10 mM PBS. A saturated solution of PBS with 1-octanol was prepared by mixing 16 mL of PBS with 4 mL of 1-octanol. The saturated solutions were shaken for 24 h at ambient temperature ($\approx$22 °C) using a New Brunswick Classic C25KC Incubator Shaker set at 230 rpm before further use. Starting with 500 μL of 50 μM complex (chloride salt) prepared in saturated 1-octanol, an equal volume of saturated water was added to give a total volume of 1 mL. The mixtures were shaken 200 times, centrifuged at 11 000 rpm ($\approx$10 000 × g) for 2 minutes using a BioRad Model 16K Microcentrifuge; the two resultant layers were then separated with a syringe. The concentrations of the complexes in both octanol and water layers were calculated from absorption measurements using a microplate reader (SpectraMax M2e) and standard curves in each solvent.

2.5 Computational details

The photophysical properties and the feasibility of Type I and Type II photoreactions of Os(II)-compounds were explored at DFT and TDDFT levels of theory,[68] as implemented in Gaussian09 code.[69] Ground singlet and triplet state geometry optimizations were performed in water without constraints by using PBE0 exchange–correlation functional (XC),[70] and adopting the IEFPCM model (integral equation formalism polarizable continuum model)[71,72] to simulate the solvent environment ($\varepsilon = 80$). The Os(II) metal ion was described by using the quasi-relativistic Stuttgart–Dresden pseudopotential[73] while the 6-31+G(d,p) basis set was adopted for all the other atoms.

Absorption spectra were obtained in water on the ground state equilibrium structures, using the same basis set as for the optimizations by employing the M06 XC-functional,[74] which has been widely tested and verified in terms of its reliable prediction of the photophysical properties of metallic compounds.[75] The selected protocol allows a direct comparison with results previously obtained for analogous Ru(II)-compounds.[76]

2.6 Spectroscopy

Spectroscopic measurements were obtained from dilute (5–20 μM) solutions of the PF_6^- salts of the complex in spectroscopic grade MeCN that had been further distilled over CaH_2 under argon. Deaerated solutions were prepared by five freeze–pump–thaw repetitions in custom Schlenk-style quartz cuvettes (10 mm path length) for transient absorption measurements and by sparging with argon in septum-capped quartz cuvettes (10 mm path length) for emission. Ambient air was bubbled through solutions to be used for singlet oxygen measurements.

2.6.1 UV-visible spectroscopy. UV-vis absorption spectra were recorded using a Jasco v730 spectrometer with 5 mm path length quartz cuvettes. Molar extinction coefficients (ε) were calculated at local peak maxima by regressing absorption *versus* concentration for five concentrations.

2.6.2 Emission spectroscopy. Steady-state emission spectra were measured on a PTI Quantamaster spectrometer equipped with a K170B PMT for UV to NIR (limit around 800 nm) wavelengths Hamamatsu R5509-42 NIR PMT detector having a useable detection range of around 600–1400 nm. The spectra were internally corrected for wavelength-dependent variations in source output and detector sensitivity. The most intense longest-wavelength peak in the excitation spectrum was used for this measurement.

2.6.3 Singlet oxygen. Quantum yields for singlet oxygen sensitization (Φ_Δ) were measured *via* the intensity of the $^1O_2$ emission at around 1276 nm, using $[Ru(bpy)_3](PF_6)_2$ as a standard ($\Phi_\Delta = 0.56$ in aerated MeCN),[77] by the relative actinometric method shown in eqn (1), where I denotes the integrated emission intensity, A is the absorbance of the UV-vis spectrum at the excitation wavelength, and η is the refractive index of the solvent. The subscript S denotes the standard.

$$\Phi_\Delta = \Phi_{\Delta,S}\left(\frac{I}{I_S}\right)\left(\frac{A_S}{A}\right)\left(\frac{\eta^2}{\eta_S{}^2}\right) \quad (1)$$

The Φ_Δ experiments were performed in triplicate for MeCN solutions of the PF_6^- salts. MeCN was used because water quenches the $^1O_2$ emission, and PF_6^- salts in MeCN are commonly used in the literature for comparison. The excitation wavelength was the longest wavelength in the excitation spectrum that maximized emission at 1268 nm. The emission was collected between 1200–1350 nm using a 1000 nm long-pass filter. Values were generally reproducible within ±5%.

2.6.4 Transient absorption spectroscopy. Nanosecond transient absorption (TA) lifetimes and differential excited absorption (ESA) spectroscopy were performed on an Edinburgh Instruments LP-980 spectrometer equipped with the PMT-LP detector. The third harmonic of a Continuum Minilite Nd:YAG laser provided 355 nm excitation (0.1 Hz, ≈5 ns pulse width, ≈7–9 mJ per pulse). ESA spectra were recorded between 350–750 nm in 10 nm intervals and were corrected to remove any contribution from emission. TA lifetimes were measured at single wavelengths with a bandwidth selected for optimal detector response, and fit to mono- or multiexponential decays with the instrument's L900 software or Gnuplot. This apparatus was also used to measure phosphorescence lifetimes.

2.7 Cellular assays

2.7.1 Metal compound solutions. Stock solutions of the chloride salts for $[Os(phen)_3]^{2+}$, **Os-*n*T** (n = 0–3), and $[Ru(bpy)_2(dppn)]^{2+}$ were prepared at 5 mM in 10% DMSO in water. **Os-4T** was prepared at 25 mM in DMSO due to limited solubility in the former solvent. Cisplatin was prepared at 5 mM in water and heated to dissolution. All stock solutions were stored at −20 °C prior to use. Working solutions were prepared as serial dilutions in 1× Dulbecco's phosphate-buffered saline without Ca^{2+} or Mg^{2+} (diluted and sterifiltered from 10× DPBS, Corning 20-031-CV). Cellular assays involved less than 1.2% v/v DMSO at the highest complex concentration.

2.7.2 Cytotoxicity and photocytotoxicity. All cell culture was performed as previously described for SK-MEL-28 malignant melanoma cells (ATCC HTB-72).[41] Murine B16-F10 melanoma cells (ATCC CRL-6475) were cultured in a similar manner with the exception that DMEM was used *in lieu* of EMEM. Cell lines were generally assayed within 5 passages or 10–15 passages from receipt of seed stock.

2.7.2.1 Normoxia. Cell viability experiments in normoxia were performed and data analyzed as previously described.[23,41] The light treatments used for full dose–response included cool white visible (400–700 nm; maximum ≈450 nm), green (523 nm), and red (633 nm) light at an irradiance of 20 mW cm^{-2} for a total fluence of 100 J cm^{-2}. External validation experiments were specific to Acadia University and used a broadband BenQ projector visible light source and red (630 nm) LED panel at an irradiance of 33–40 mW cm^{-2} for a total fluence of 100 J cm^{-2}. Plates were read with a Molecular Devices M2e (λ_{exc} = 530 nm, long-pass 570 nm, λ_{em} = 620 nm) at UNCG/UTA or a Cytofluor 4000 ($\lambda_{exc/em}$ 530 ± 25/620 ± 40 nm) reader at Acadia University.

Specialized dosimetry experiments on the Modulight ML8500 platform included well-by-well illumination with lasers centered at 525, 630, and 753 nm at various fluences (0–400 J cm^{-2}) and

constant irradiance of 300 mW cm^{-2}. Additional experiments with **Os-4T** included 384-well plates using (a) illumination with a CivilLaser 733 nm laser (~5 mW cm^{-2}) in tandem with a frontal diffuser by Medlight (model FD Frontal Light Distributor) and (b) monitoring **Os-4T** performance over a month with varying conditions (pipette tip, cell parent seed stock, plate map). The assay procedure for a 384-well plate is outlined in SI method SM-1. The spectral profiles of the light sources are shown in Fig. S-22 and S-23.† Spectral output was monitored using the Luzchem SPR fiber optic detector in tandem with an Ocean Optics USB4000 spectrophotometer and an Ocean Optics UV-Vis XSR fiber optic of 230 μm diameter. Irradiance was measured using a Thorlabs Optical Power Meter PM100D and their corresponding thermal power sensor S310C. Irradiance was generally within 5% across entire plate area for full-plate illumination.

2.7.2.2 Hypoxia. Cell culture and compound evaluation in hypoxia were performed as previously reported for SK-MEL-28 cells.[41] Only SK-MEL-28 cells and full dose–response experiments (EC_{50} determination) were applied in hypoxia for comparison to normoxic data. As in our previous work, resazurin-based cell viability endpoints had strong interference on hypoxia-treated well plates. An additional sulforhodamine B (SRB) endpoint was included for any hypoxic assay comparisons due to lack of compound interference at lower concentrations. Comparisons of results with resazurin *versus* SRB and the required corrections are shown for both oxygen treatments in Fig. S-24.† Following resazurin reads, the plates were treated in accordance with the precedent literature.[78–80] Well plates were briefly centrifuged in a prechilled (4 °C) Thermo Scientific™ Sorvall™ Legend™ RT centrifuge with swinging bucket rotor (7500 6445, 7500 6449) at 180 × *g* for 5 min. Protein was precipitated by incubation for 45 min to 1 h with final 10% w/v trichloroacetic acid (TCA, pre-chilled) per well at 4 °C. Supernatant was removed *via* simple plate inversion and flick. Precipitate was washed five times with 150–200 μL per well DI water at ambient temperature. Afterwards, protein was stained with 50 μL per well of 1 mM SRB in 1% v/v acetic acid, briefly incubated for 15–30 min at ambient temperature (~20 °C), and washed five times with 200 μL per well of 1% v/v acetic acid.

Protein was finally dissolved in 200 μL per well of 10 mM Trizma base. Well solutions were read after 1 h incubation at 565 nm. Note that shorter incubation times can be used with a plate shaker. Alternative endpoints (510 nm abs. or fluorescence) were also explored but found to be less selective for SRB due to spectral overlap with the metal complexes. Day 0 reference plates were prepared, and values subtracted from final readings to test treatment effect on relative changes in protein. Rather than use as a true cytotoxicity assay as sometimes ascribed, SRB results were interpreted similarly to the NCI60 panel,[81] as a reference to the cell death response.[80] Interpolated endpoints are as follows:

$$GI_{50} = \left(\frac{T - T_0}{C - T_0}\right) \times 100\% = 50\% \quad (2)$$

$$LC_{50} = \left(\frac{T - T_0}{T_0}\right) \times 100\% = -50\% \quad (3)$$

$$TGI = \left(\frac{T - T_0}{C - T_0}\right) \times 100\% = 0\% \quad (4)$$

where GI_{50} is the concentration that causes 50% growth inhibition at the assay end (T) relative to the difference of the positive growth control (C) and day of compound addition (day 0, T_0). LC_{50} is a measure of cytotoxicity based on 50% reduction of protein relative to day 0. Lastly, TGI is the concentration at which there is total growth inhibition. In this respect, both the LC_{50} and TGI can be used to confer a cytotoxic effect. The negative growth control (no cells or compound) was subtracted prior to any further processing. All values were interpolated against logistic 4-parameter sigmoidal curves.

For the longitudinal study or repeats of (photo)cytotoxicity experiments (normoxic and hypoxic) with **Os-4T** in SK-MEL-28, resazurin was used as the viability indicator. Results were plotted with original run (repeat #0) using log scale EC_{50} and PI values to monitor change over time. Repeats 1–5 were conducted within a month of each other in 384 well-plates (see SM-1); the study began several months after the original run (repeat 0) in 96-well-plates. Variables were adjusted as follows to simulate differences common in assay comparisons across long periods of time. Repeats used different plate maps (all), different tips (Sartorius 790352 repeats #0–1, VWR 83007-352 repeats #2–3, low retention Sartorius LH-L790352 repeats #4–5), changed cell parent seed stock for repeats 4–5, and overhead lights were off in #5. Serum and consumable lots were identical for repeats 1–5. Cell passage numbers were equal and between 10–15 passages from seed stock receipt.

2.8 Maximum tolerated dose in mice

An 8 week old litter of female C57BL/6J mice, averaging 20 g per mouse, were treated by intraperitoneal injection of **Os-4T** in accordance with protocol A20-006 (approved by WFU Animal Care and Use Committee). Mice were dosed from 25–200 mg kg^{-1} with 200 μL injections and 10% DMSO in 0.9% saline as the vehicle. Solutions of **Os-4T** were prepared immediately with sonication before injection. Female mice were dosed by slow intraperitoneal injection (the lower right abdominal quadrant) only after visible confirmation of complete compound dissolution. Animals were continuously monitored for 2 hours, frequently over the next 6, and periodically for up to 2 weeks before being sacrificed. Mice were accordingly euthanized if (a) a combination of moderate severity signs appeared, (b) a single severe sign appeared, or (c) the study period was complete, 2 weeks post-injection. The maximum tolerated dose (MTD) was defined as the dose that produces moderate signs of clinical toxicity in the final tested animal.

3. Results and discussion

3.1 Synthesis and characterization

Complexes $[Os(phen)_2(IP\text{-}nT)]^{2+}$ **Os-0T–Os-4T** were synthesized following adapted literature procedures.[82–84] The complexes were isolated as their PF_6^- salts and purified with flash chromatography on silica, affording final products in 16–60% yields. The PF_6^- salts were converted to their corresponding Cl^- salts

in quantitative yields *via* anion metathesis using Amberlite IRA-410 and were further purified using size-exclusion chromatography on Sephadex LH-20, if needed. HPLC analysis confirmed the purities of complexes **Os-0T–Os-4T** to be 95% or higher (Fig. S-17–S-21†). The structures of complexes **Os-0T–Os-4T** were confirmed using high resolution ESI^+ mass spectrometry (Fig. S-11–S-15†) and a detailed analysis of their 1D ^1H NMR (Chart 2 and Fig. 1) and 2D ^1H–^1H COSY NMR spectra (Fig. S-2–S-6†). Assignments were made based on the connectivities observed in ^1H–^1H COSY NMR and in consultation with literature sources.[65,66] Compound **Os-4T** required additional ^{13}C, ^{13}C–^1H HSQC, and ^{13}C–^1H HMBC NMR experiments for full assignment of the ^1H NMR signals of the quaterthiophene group (Fig. S-7–S-9†). The chemical shifts and resolution of signals from the thiophene ring hydrogens exhibited a concentration dependence, especially for complexes with longer thiophene chains. The best resolution of these NMR signals was obtained at concentrations near 1.6 mM.

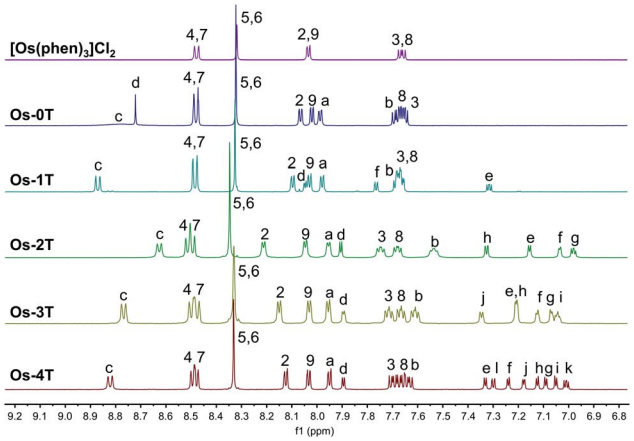

Fig. 1 500 MHz ^1H NMR spectra of reference compound $[Os(phen)_3]Cl_2$ and **Os-0T–Os-4T** (Cl^- salts) in MeOD-d_3 at 298 K, aromatic region.

3.1.1 Determining NMR assignments for complexes Os-0T–Os-4T. The hydrogen labels used in ^1H peak assignments of $[Os(phen)_3]Cl_2$ and complexes **Os-*n*T** (n = 0–4) are shown in Chart 2. Tris-homoleptic $[Os(phen)_3]Cl_2$, which was characterized in detail by Pazderski *et al.*,[66] was used to establish the positions of the signals from hydrogens 2–9 in complexes **Os-0T–Os-4T**. Hydrogens 2 and 9 were the most distinct from each other among these four pairs. While literature assignments have placed the chemical shift for hydrogen 2 upfield to that of 9 for similar complexes,[85–88] we assign the signal for 2 downfield to that of 9 in the **Os-*n*T** series based on the systematic changes in the chemical shifts of 2 and 9 with variation of n. Throughout the **Os-*n*T** complex series, the chemical shift of 9 was relatively unchanged and closely matched the chemical shift of the 2,9-signal in the $[Os(phen)_3]^{2+}$ complex, while hydrogen 2 shifted downfield relative to the chemical shift of 2,9-signal in $[Os(phen)_3]^{2+}$, with the difference in chemical shifts of 2 *versus* 9 in **Os-*n*T** series being the most pronounced in the complexes with longer thiophene chains. The difference in chemical shifts of 2 and 9 was attributed to changes in the proximal magnetic environment of 2. While hydrogen 9 is shielded by the π-system of a neighboring phenanthroline ligand, hydrogen 2 is shielded by the π-system of the neighboring IP-*n*T ligand. The shielding strength of the phenanthroline ligand remains constant throughout the **Os-*n*T** series (and is the same as the shielding strength of the phenanthroline ligand in homoleptic complex $[Os(phen)_3]^{2+}$), which agrees with the observation that the chemical shift of 9 did not change throughout the series. However, as n varies, the shielding strength of the IP-*n*T ligand changes and thus the chemical shifts of the signals for hydrogen 2 change as a result. As the signal for hydrogen 2 was downfield of 9 in all **Os-*n*T** complexes, it was hypothesized that the magnitude of the shielding effect by the IP-*n*T ligand is smaller than that of

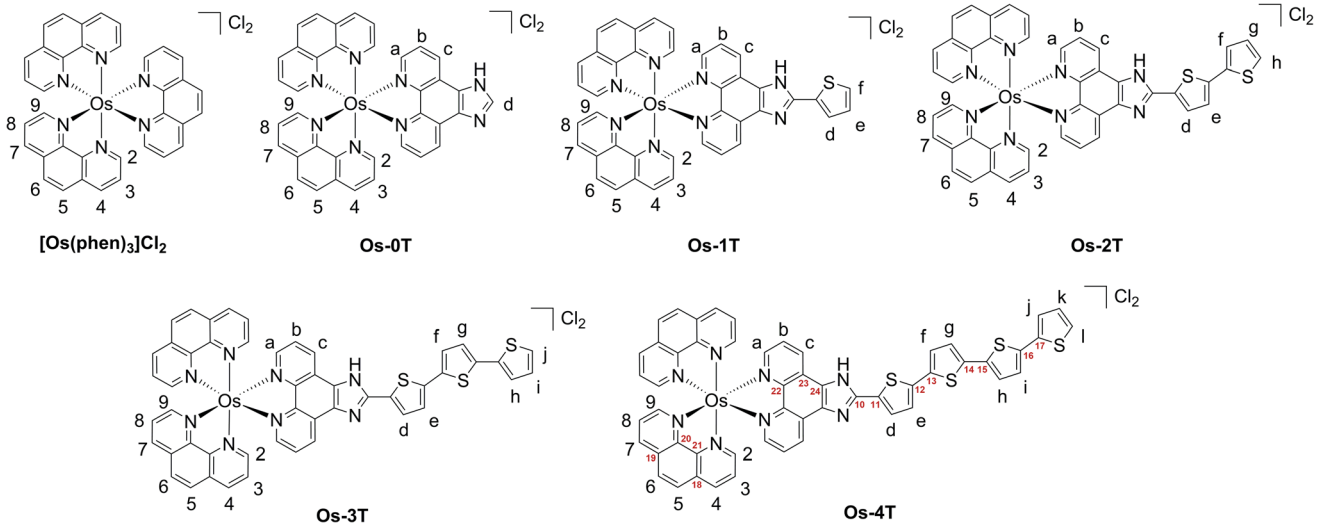

Chart 2 Hydrogen labels (black) and selected carbon labels (red) used in ^1H peak assignments of reference compound $[Os(phen)_3]^{2+}$ and **Os-0T–Os-4T**.

phenanthroline, most likely due to delocalization of the electron density into the more extended π-system of the IP-*n*T ligand. A similar, but less pronounced, phenomenon was observed for hydrogens 3 and 8. The chemical shift of hydrogen 8 remained unchanged and closely matched the chemical shift of the 3,8-signal in the $[Os(phen)_3]^{2+}$ complex, while hydrogen 3 shifted downfield in complexes with more thiophenes. Hydrogens 4,7, which are positioned further away from the shielding influence of the phenanthroline and IP-*n*T ligands, were notably less affected and, as a result, overlap when $n = 0$–1. The signal for hydrogen 4 shifts only slightly more downfield relative to that for 7 when $n = 2$–4. Hydrogens 5,6 are positioned outside of the shielding influence of the neighboring ligands and appear nearly equivalent as a singlet for $n = 0$–4 that resembles the 5,6 singlet in the spectrum for $[Os(phen)_3]^{+2}$.

The a–b–c spin system was assigned next. It appeared as c > a > b, repeating the pattern observed for spin systems 2–3–4 and 7–8–9, where the signal for the hydrogen in the *meta*-position relative to the Os-coordinated nitrogen was shifted the farthest upfield and that for the hydrogen in the *para*-position appeared the most downfield of the three. Due to similarities between these spin systems, a appeared close to 2,9, and b appeared close to 3,8, and c appeared relatively close to 4,7. The signal for the imidazole-NH hydrogen was not observed, in agreement with the literature,[85,86,89] where quick exchange between the two nitrogens of the imidazole ring occurs in solution.

In thiophene-containing complexes **Os-1T–Os-4T**, the signals from the thiophenes integrated as one hydrogen each and were assigned last. Among those, three hydrogen signals were most diagnostic. The signal for hydrogen d was the most downfield compared to the signals for the rest of the thienyl hydrogens due to the strong deshielding effect of the nitrogens of the neighboring imidazole. Another strongly deshielded hydrogen was the hydrogen positioned closest to the sulfur (f in **Os-1T**, h in **Os-2T**, j in **Os-3T**, and l in **Os-4T**). The signal for the most shielded hydrogen appeared as a distinct doublet of doublets and corresponded to the middle hydrogen of the most distal thiophene ring (e in **Os-1T**, g in **Os-2T**, i in **Os-3T**, and k in **Os-4T**). Using these characteristic signals as starting points, the rest of the thiophene signals from the proximal and the most distal thiophene ring were assigned *via* the observed ^1H–^1H COSY correlations.

Assigning the signals from the internal thiophenes was less straightforward and was accomplished for **Os-4T** with the aid of ^{13}C–^1H HSQC and ^{13}C–^1H HMBC NMR experiments (Fig. S-8 and S-9†). The two internal spin systems (f–g and h–i) were first established using ^1H–^1H COSY correlations. Then, ^{13}C–^1H HSQC was used to identify which ^{13}C peaks corresponded to the thiophene hydrogens d–l. Then, ^{13}C–^1H HMBC was used to establish diagnostic correlations, starting with hydrogens d and e. Hydrogens d and e both correlated to two of the same ^{13}C peaks (132.20 ppm and 141.39 ppm), which were assumed to be carbons 11 and 12. Hydrogen d correlated more strongly to the peak at 132.20 ppm, and hydrogen e correlated more strongly to the peak at 141.39 ppm, which allowed for carbon 11 and carbon 12 to be assigned as signals at 132.20 ppm and 141.39 ppm, respectively. In addition to correlations with d and e, carbon 12 exhibited correlations with one more hydrogen, which led to the assignment of this hydrogen as f. Hydrogen g was then readily identified *via* its correlation to f in the ^1H–^1H COSY NMR spectrum. Next, a diagnostic ^{13}C signal at 137.79 ppm exhibited correlations to hydrogens l, j, and one more ^1H signal that was assigned as hydrogen i. This ^{13}C signal was assigned as carbon 17 due to the greatest possibility of both l and j showing correlation to it. Lastly, hydrogen h was then readily identified *via* its correlation to i observed in the ^1H–^1H COSY NMR spectrum.

3.2 Lipophilicity

The lipophilicities of the chloride salts of the compounds, including the reference $[Os(phen)_3]Cl_2$, were evaluated by determining their log $D_{o/w}$ values (Fig. 2 and Table S-1†). This parameter reflects the solubility preference of a given compound for either octanol or aqueous PBS prepared at neutral pH, where positive values indicate higher lipophilicity (octanol solubility) and negative values indicate lower lipophilicity (aqueous solubility).[90] Among the series, the log $D_{o/w}$ values increased systematically with the number of thienyl rings appended to the IP ligand. The compounds were essentially hydrophilic from $n =$ 0 to 2 (**Os-0T–Os-2T**), with an abrupt switch to lipophilic at $n = 3$ (**Os-3T**). **Os-0T** was the only compound that was more hydrophilic than $[Os(phen)_3]Cl_2$, reflecting the influence of the imidazo group of the IP ligand (relative to phen) on aqueous solubility. The difference in lipophilicities for **Os-0T**, lacking thienyl groups, to three in **Os-3T** was approximately 10^3. The log $D_{o/w}$ value for **Os-4T** could not be determined owing to its precipitation from the solvent mixture under all conditions, suggesting an even greater lipophilicity that favors self-aggregation through favorable π–π interactions.

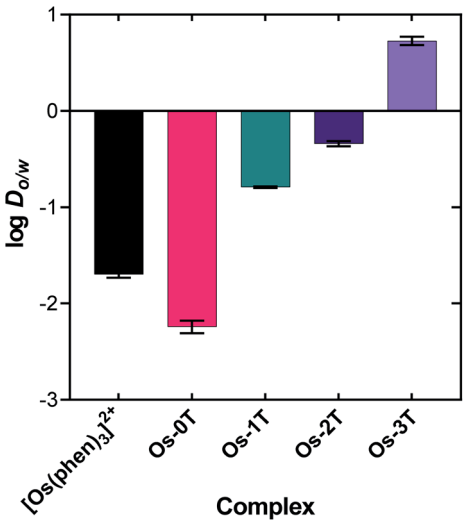

Fig. 2 Octanol–water distribution coefficients (log $D_{o/w}$ ± SD) for reference compound $[Os(phen)_3]^{2+}$ and **Os-0T–Os-3T** (Cl^- salts); SD = standard deviation. The value of log $D_{o/w}$ for **Os-4T** could not be determined due to its precipitation from the solvent mixture.

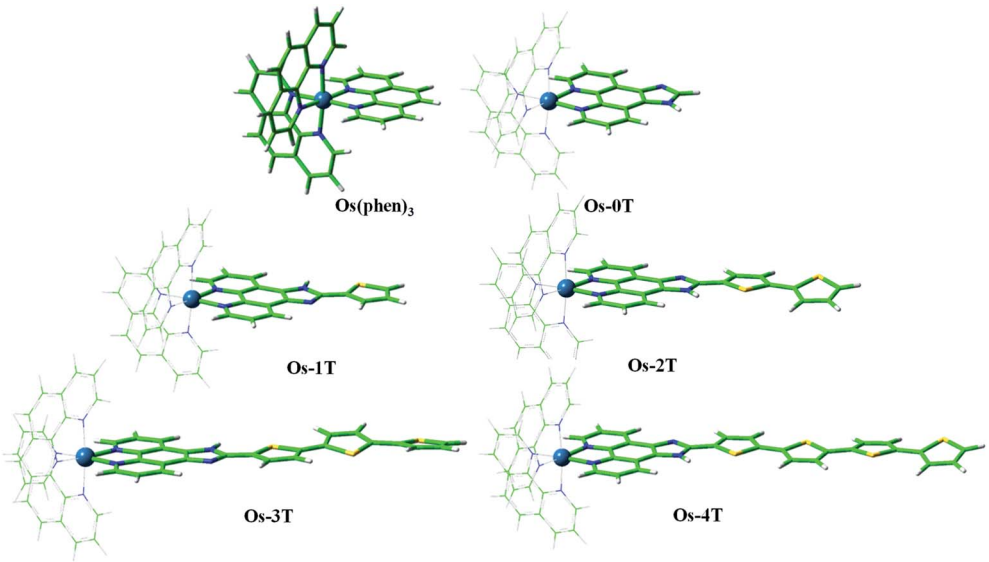

Fig. 3 Optimized geometries of reference compound $[Os(phen)_3]^{2+}$ and **Os-0T–Os-4T** in a water environment at the PBE0/6-31+G**/SDD/ level of theory.

3.3 Computational studies

3.3.1 Calculated ground state electronic structures and UV-vis spectra. A computational investigation of the ground and excited states of $[Os(phen)_3]^{2+}$ and the **Os-*n*T** dications in water was carried out using DFT and TDDFT calculations. Optimized geometries for the singlet ground state indicate that the central metal ion is surrounded by its ligands in a pseudo-octahedral environment throughout the series and that the thiophene rings adopt a coplanar *trans* conformation (Fig. 3 and Table S-2†). The calculated ground state structures indicated that the planarity of the rigid IP ligand extends to the first electron-donating thiophene ligand. Each additional thienyl group (n = 2–4) appended to the coordinated IP ligand is conformationally more flexible, with the terminal thiophene ring being twisted by up to 18° with respect to the plane of the first thiophene ring.

The ground state electronic structures of these complexes can be described by the frontier molecular orbitals (HOMO−1, HOMO, LUMO, LUMO+1) shown in Fig. S-27–S-31.† The calculated percent contribution of the Os d-orbitals, phen, IP and thienyl chain to the frontier orbitals of each complex in the singlet ground state are reported in Table 1. The nature of the HOMO (Fig. 4) changed with the number of thienyl groups in the chain. The considerable amount of Os d character (~35%) in the HOMO of $[Os(phen)_3]^{2+}$, **Os-0T** and **Os-1T** nearly vanished (<5%) when two or more thiophenes were incorporated. The increasing contribution of the distal thiophene rings to the HOMO is illustrated by the energy trend plot in Fig. 5a. For **Os-2T** through **Os-4T**, the HOMO orbital becomes progressively more ligand-based and reaches a maximum value for thienyl contribution in **Os-4T**. The incorporation of a polythiophene chain (with $n \geq 2$) thus, produces the installation of a HOMO orbital of organic character lying at higher energies, reflected by the HOMO–LUMO gaps shown in Fig. 5a and the HOMO orbital plots in Fig. 4. By sharp contrast, the composition of the HOMO−1 orbital was relatively unchanged throughout the series (Fig. S-28†), being largely comprised of Os d character (30–39%) mixed with phen and IP (61–68%) but without any contribution from the thiophene chains.

The lowest unoccupied molecular orbitals (LUMOs and LUMO+1s, Fig. S-29 and S-30†) were almost exclusively localized to the phen and IP (phen portion) ligands. The contribution of

Table 1 Calculated percent contribution of the Os d-orbital, phen, IP and thienyl chain to the frontier orbitals (HOMO−1, HOMO, LUMO, LUMO+1) of reference compound $[Os(phen)_3]^{2+}$ and **Os-0T–Os-4T** in the singlet ground state ^{1}GS

	HOMO−1				HOMO				LUMO				LUMO+1			
%	Os	Phen	IP	Thienyl	Os	Phen	IP	Thienyl	Os	Phen	IP	Thienyl	Os	Phen	IP	Thienyl
$[Os(phen)_3]^{2+}$	36	64	—	—	35	65	—	—	3	97	—	—	2	98	—	—
Os-0T	39	42	19	0	34	46	19	0	3	59	39	0	4	69	28	0
Os-1T	30	34	34	2	34	40	25	0	3	59	39	0	3	72	25	0
Os-2T	34	35	31	0	4	47	24	25	3	57	38	3	4	57	24	15
Os-3T	34	40	25	0	1	38	17	45	3	57	39	1	7	42	25	26
Os-4T	35	42	23	0	1	32	13	55	3	54	40	3	8	42	28	22

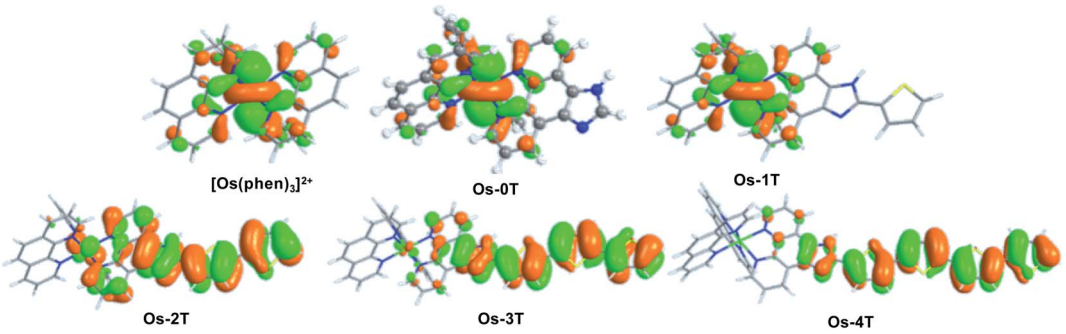

Fig. 4 HOMO orbital plots for reference compound $[Os(phen)_3]^{2+}$ and **Os-0T–Os-4T**, calculated in water at M06/6-31+G(d,p)/SDD/level of theory.

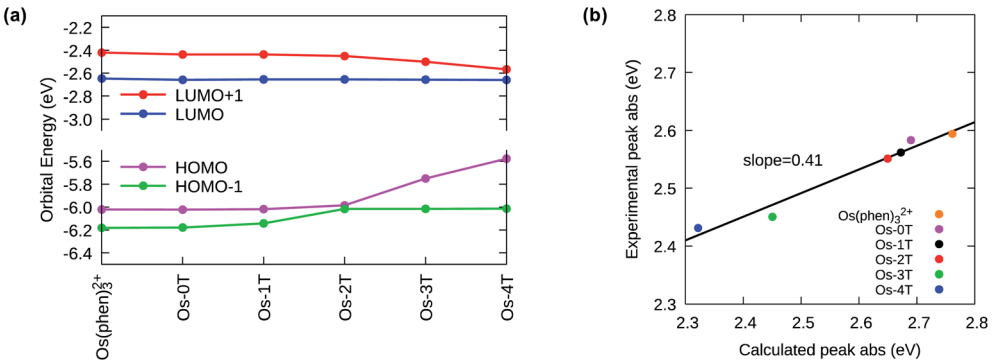

Fig. 5 (a) Calculated frontier orbital energies for reference compound $[Os(phen)_3]^{2+}$ and **Os-0T–Os-4T**. (b) Correlation of calculated and experimental longest wavelength absorption maxima for reference compound $[Os(phen)_3]^{2+}$ and **Os-0T–Os-4T** measured in water.

the thienyl chain produced opposite effects on the HOMO *versus* LUMO+1 orbitals and had almost no effect on the LUMOs (Fig. 5a). While the energy of the LUMO orbital remains constant with the same % composition regardless of the number of thienyl groups, the LUMO+1 drops slightly in energy with ≥2 thiophene rings, consistent with an increased contribution from the thienyl ligand observed in the orbital composition (15, 26 and 22% in **Os-2T**, **Os-3T** and **Os-4T**, respectively).

The increase of the HOMO and concomitant decrease of the LUMO+1 energies with n is reflected in the calculated UV-visible absorbance spectra of the **Os-*n*T** series (Fig. 5b, S-32, S-33 and Table S-3†). There is a clear and systematic increase in the absorption intensity throughout the visible region with increasing n on going from **Os-0T–Os-4T**, reaching singlet–singlet transition energies into the red.

Close inspection of the computed transitions and their orbital compositions allowed assignment of the orbital parentage and configuration of the experimental lowest-energy spin-allowed, singlet–singlet bands in the UV-vis absorption spectra (*i.e.*, transitions occurring <550 nm). There was an abrupt change in the nature of these lowest-energy spin-allowed transitions with $n > 2$, which reflected the decreased contribution of the metal-based orbitals and increased contribution of the thienyl-based orbitals to the lowest-energy singlet–singlet electronic transitions as thiophene rings were added. The lowest-energy transitions had predominantly ^{1}MLCT character for $n \leq 2$ (**Os-0T–Os-2T**), while ^{1}ILCT character made a significant contribution to those with $n \geq 3$ (**Os-3T**, **Os-4T**) where the HOMO orbital was exclusively localized over the thienyl groups. This change in the nature of the lowest-energy spin-allowed transitions was also supported by a solvent dependence (water *versus* acetonitrile, Fig. S-35†) in the experimental absorption spectra for **Os-3T** and **Os-4T** but not for **Os-0T–Os-2T**.

Os-3T showed an intense band contributed mostly by a transition centered at 484 nm (*versus* an experimental value of 487 nm) characterized as ILCT (48%) mixed with MLCT (29%), and another intense band near 506 nm, which was also mixed ILCT/MLCT (Table 2 and Fig. S-33†). **Os-4T** had its most intense band bathochromically shifted to 534 nm and was unequivocally assigned to ILCT. The charge-transfer nature of these ligand-localized $^1\pi\pi^*$ transitions in **Os-3T** and **Os-4T** was corroborated by the solvent dependence of these transitions in the experimental absorption spectra (Fig. S-34 and S-35†).

3.3.2 Excited state calculations and feasibility of Type I and Type II photoreactions. The geometries of the lowest-energy triplet excited states for the Os(II) IP-*n*T (n = 1–4) complexes were calculated and compared to their singlet ground state conformations (Fig. S-25, S-26 and Table S-2†). There were no differences in the Os(II) coordination sphere or the Os–N bonds between the ground and triplet excited states. However, it is known that the excited states of oligothiophenes adopt quinoid type structures that are essentially planar with maximal π-

Table 2 Theoretical peak assignments for **Os-0T–Os-4T**

Complex	λ_{max} calc	λ_{max} exp	Transitions	Assignment
Os-0T	461	480	H−1 → L+1 (45%) H−2 → L+2 (37%)	MLCT
Os-1T	464	484	H−1 → L+1 (49%) H−2 → L+2 (41%)	MLCT
Os-2T	468	486	H−2 → L+2 (44%)	MLCT
Os-3T	506	506	H−3 → L (48%) H → L (38%)	MLCT + ILCT
	484	487	H → L+1 (48%)	ILCT
Os-4T	534	520	H → L+1 (55%) H → L (34%)	ILCT
	451	436	H−1 → L+5 (52%)	MLCT

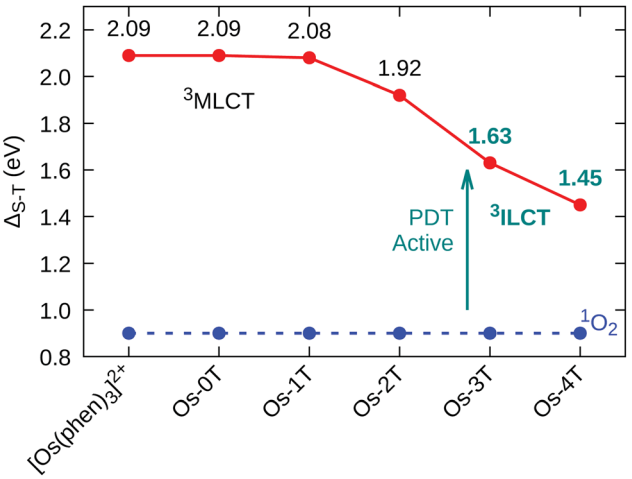

Fig. 6 Singlet–triplet energy gap (Δ_{S-T}) for reference compound [Os(phen)$_3$]$^{2+}$ and **Os-0T–Os-4T**, in water, at the M06/6-31+G(d,p)/SDD level of theory.

conjugation.[91,92] For the IP ligands appended with *n*T groups, this was also the case. The dihedral angles (φ_n) for the excited state triplets states were within 1° of the fully planar 180° conformation. The conformational changes that occur on going from the ground state to the excited triplet state were more pronounced in the terminal thienyl group in each case. Across the series the more π-extended oligothiophene chains were subject to the largest conformational changes between the ground and excited state, with the most dramatic differences for **Os-3T** and **Os-4T** where rotational changes of around 18° were calculated.

The nature of the lowest-lying triplet states of the **Os-*n*T** dyads was examined by Mulliken spin density (MSD) calculations and was found to vary among the series. The MSD on the Os(II) center for complexes with $n \leq 2$ was one, indicative of one unpaired electron on the metal center as would be expected for the ^{3}MLCT state. No involvement of the metal was detected for **Os-3T** and **Os-4T**, supporting the assignment of the lowest-energy triplet states in these two complexes as the ^{3}ILCT state. The installation of low-lying ^{3}ILCT states for **Os-3T** and **Os-4T** can be thus connected with greater π expansion, which was also responsible for a drop in the triplet state energy. The calculated T_1 state energies of [Os(phen)$_3$]$^{2+}$, **Os-0T**, and **Os-1T** were nearly identical (≈2.09 eV), but decreased systematically with added thiophene rings, falling to 1.45 eV in **Os-4T** (Fig. 6). Earlier work has connected similar stabilization of the ^{3}ILCT energy with longer lifetimes in Ru(II) complexes,[57,93,94] and this could account for **Os-4T** having exceptional *in vitro* activity (*vide infra*).

The capacity of the triplet-state Os(II) complexes to promote Type I and Type II photoreactions was explored. To produce the cytotoxic singlet oxygen species, the singlet–triplet splitting energy of the complex must be larger than that of O_2, thereby allowing energy transfer to promote the O_2 $^3\Sigma_g^- \rightarrow {}^1\Delta_g$ transition; the lowest oxygen singlet state energy was previously computed to be 0.90 eV,[95] in good agreement with the experimental value of 0.98 eV. The calculated singlet–triplet energy gaps (Δ_{S-T}) show that every compound in the series is sufficiently energetic to form $^1O_2$ through a Type II pathway (Fig. 6).

There also exists the possibility that the triplet state could generate the superoxide anion $O_2^{\bullet-}$ through Type I photoreactions. This is a potentially important process since $O_2^{\bullet-}$ can participate in rapid bimolecular reactions that lead to other reactive oxygen species (ROS) such as H_2O_2 and OH$^\bullet$, which in turn could damage biomolecules.[95] The $O_2^{\bullet-}$ species can be formed by direct electron transfer from the photosensitizer (PS) to O_2 (5), or by an electron transfer mechanism from a reduced form of the PS to O_2 (6). The reduced form of the PS could be generated by autoionization reactions (7) and (8), through the reduction of a PS T_1 state by a neighboring PS in the S_0 or T_1 state. Such reactions were explored computationally through the vertical electron affinity (VEA) and ionization potentials (VIP) of each Os(II) compound and for molecular oxygen.[76,96–98] The results are summarized in Table 3.

$$PS(T_1) + {}^3O_2 \rightarrow PS^{\bullet+} + O_2^{\bullet-} \quad (5)$$

$$PS^{\bullet-} + {}^3O_2 \rightarrow PS + O_2^{\bullet-} \quad (6)$$

$$PS(T_1) + PS(S_0) \rightarrow PS^{\bullet+} + PS^{\bullet-} \quad (7)$$

$$PS(T_1) + PS(T_1) \rightarrow PS^{\bullet+} + PS^{\bullet-} \quad (8)$$

The feasibility of direct electron transfer to molecular O_2 through reaction (5) decreases as the thiophene chain grows, as was previously observed for the related Ru(II) complexes.[76] The triplet states of the Os(II) complexes become weaker electron

Table 3 VEA and VIP values (eV) in water for $^3O_2$ molecule, and for reference compound [Os(phen)$_3$]$^{2+}$ and **Os-0T–Os-4T** in their singlet and triplet states, computed at PBE0/6-31+G**/SDD. The O_2 electron affinity (−3.42 eV) was calculated at the same level of theory

	[Os(phen)$_3$]$^{2+}$	Os-0T	Os-1T	Os-2T	Os-3T	Os-4T
VEA	−2.92	−2.94	−2.94	−2.94	−2.94	−2.94
VIP	5.52	5.51	5.51	5.68	5.43	5.26
VEA(T_1)	−5.01	−5.03	−5.02	−4.86	−4.57	−4.39
VIP(T_1)	3.43	3.42	3.43	3.76	3.80	3.81

donors with increasing n, thus preventing the direct electron transfer process in water. This process could be possible for $[Os(phen)_3]^{2+}$, **Os-0T** and **Os-1T** but can be ruled out for **Os-2T–Os-4T** since the sum of VIP(T_1) of the latter compounds and the electron affinity of $^3O_2$ are positive.

However, the T_1 state of all the Os(II) compounds can undergo indirect Type I photoreactions. The results demonstrate that compounds in the T_1 state can be reduced through autoionization (8) with neighboring compounds in the T_1 state given that the sum of VEA(T_1) and VIP(T_1) is negative. Importantly, the higher electron affinity of oxygen compared to the Os(II)-complexes suggests that any of complexes in the reduced state is able to generate the superoxide species (6). It should be also noted that $O_2^{\bullet-}$ could behave as a further reducing agent for Os(II) T_1 states that could also be implicated in biomolecule-damaging processes, but this was not examined.

To summarize, computational studies conclude that all of the Os(II) complexes have the requisite triplet state energies to sensitize $^1O_2$ through the Type II energy transfer pathway but only $[Os(phen)_3]^{2+}$, **Os-0T** and **Os-1T** can directly form superoxide. However, all of the Os(II) complexes are capable of generating superoxide through Type I autoionization photoreactions, suggesting at least two potential modes of activity in this class of compounds. The relative contributions of these pathways in cells would likely depend on the local concentrations of these complexes and O_2 as well as the redox environment. It is possible that other intracellular mediators of electron transfer could participate in any intracellular Type I photochemistry.

3.4 Photophysical properties

The photophysical properties of the complexes were measured as dilute solutions of the PF_6^- salts in MeCN. This solvent choice facilitates comparison with related compounds in the photophysical literature.

3.4.1 Electronic absorption spectroscopy. The UV-vis spectra of the Os(II) complexes exhibit three major features in common, shown in Fig. 7 and tabulated in Table 4. Previous investigations[99,100] of $[Os(phen)_3]^{2+}$ have assigned the more intense bands between 400–525 nm (with maxima near 430 and 480 nm) to the Os(dπ) → phen(π*) MLCT transitions and the broader, weak absorption bands that taper off near 700 nm (with maxima near 660 nm) to the analogous spin-forbidden MLCT transitions. Added thiophenes did not influence these MLCT transitions (although they are somewhat obscured in **Os-3T** and **Os-4T**), which is consistent with the computational prediction that the LUMO is localized to the phen and IP ligands (Table 1). The sharper and more intense peaks near and below 300 nm were assigned to intraligand (IL) ππ* transitions on the phen/IP ligands.

Additional peaks between 330–440 nm were observed for Os(II) compounds containing thienyl groups. These absorption bands in **Os-1T** through **Os-4T** (338, 382, 413, and 436 nm, respectively) increased in intensity and decreased in energy, consistent with the increased conjugation of added thiophene

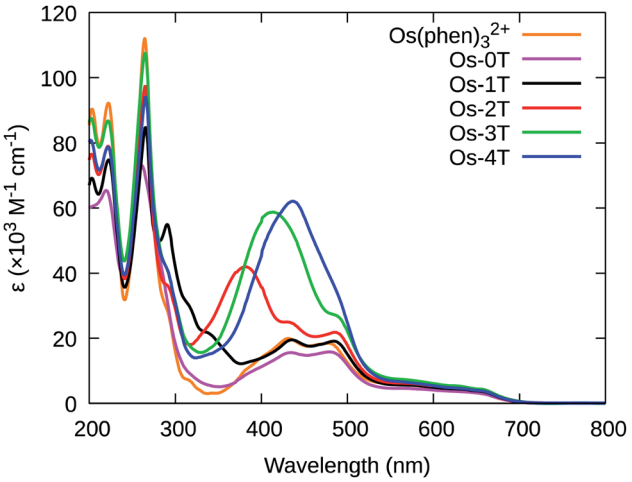

Fig. 7 UV-vis spectra of reference compound $[Os(phen)_3]^{2+}$ and **Os-0T–Os-4T** (PF_6^- salts) in room temperature acetonitrile.

Table 4 Electronic absorption data for reference compound $[Os(phen)_3]^{2+}$ and **Os-0T–Os-4T** (PF_6^- salts)

Complex	λ_{abs}/nm (log ε)[a]
$[Os(phen)_3]^{2+}$	222 (4.97), 265 (5.05), 431 (4.30), 478 (4.27), 653 (3.56)
Os-0T	220 (4.82), 261 (4.87), 434 (4.20), 480 (4.20), 655 (3.49)
Os-1T	222 (4.88), 265 (4.93), 291 (4.73), 338 (4.35), 435 (4.29), 484 (4.28), 658 (3.55)
Os-2T	222 (4.89), 265 (4.98), 288 (4.56), 382 (4.62), 432 (4.40), 486 (4.33), 658 (3.58)
Os-3T	222 (4.94), 265 (5.03), 413 (4.77), 487 (4.43), 658 (3.63)
Os-4T	222 (4.89), 265 (4.96), 436 (4.79), 656 (3.57)

[a] Absorption band maxima and extinction coefficients (M^{-1} cm^{-1}) determined in acetonitrile at room temperature.

rings, and are hence assigned to ILCT ππ* transitions involving nT of the IP-nT ligands.

3.4.2 Singlet oxygen sensitization. Quantum yields for singlet oxygen production (Φ_Δ) were measured in air-saturated MeCN solution indirectly through the intensity of the O_2 $^1\Delta_g \rightarrow {}^3\Sigma_g$ emission centered near 1268 nm (Table 5). $[Ru(bpy)_3]^{2+}$

Table 5 Emission and singlet oxygen sensitization data for reference compound $[Os(phen)_3]^{2+}$ and **Os-0T–Os-4T** (PF_6^- salts). Excitation wavelengths are indicated in parentheses. Emission lifetimes were measured following a 355 nm laser pulse (<5 ns width)

Complex	MLCT λ_{em} [λ_{ex}] (nm)	τ_{em}(ns)	Φ_Δ [λ_{ex}] (nm)
$[Os(phen)_3]^{2+}$	718 [471]	2.1×10^2	0.53 [472]
Os-0T	732 [472]	1.8×10^2	0.43 [473]
Os-1T	737 [471]	1.7×10^2	0.42 [473]
Os-2T	740 [470]	1.8×10^2	0.49 [472]
Os-3T	743 [468]	τ_1 1.4–2.9 $\times 10^2$ τ_2 3.8–7.1 $\times 10^2$	0.51 [525]
Os-4T	746 [470]	τ_1 1.8–2.2 $\times 10^2$ τ_2 1.4–1.6 $\times 10^4$	0.95 [525]

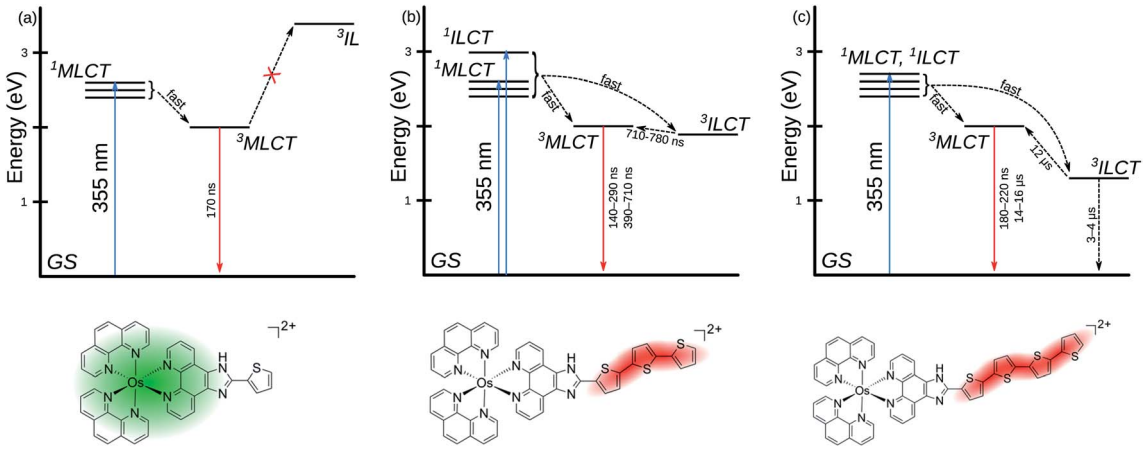

Scheme 1 Jablonski diagrams depicting the proposed decay pathways in (a) **Os-1T**, (b) **Os-3T**, and (c) **Os-4T**.

($\Phi_\Delta = 0.56$)[77] was used as the standard, in accordance with eqn (1). $[Os(phen)_3]^{2+}$ exhibited a comparable quantum yield ($\Phi_\Delta = 0.53$), and the **Os-0T–Os-3T** members of the series were similarly efficient. Unlike the other family members, **Os-4T** sensitized $^1O_2$ with near-unity efficiency, reflecting behavior that we have previously observed in related tetrathienyl complexes of Ru(II).[57]

3.4.3 Emission. All of the Os(II) family members exhibited a single broad, featureless emission in Ar-sparged acetonitrile at room temperature (Table 5 and Fig. S-36†). Incorporation of IP and IP-appended thienyl groups lowered the emission energy compared to $[Os(phen)_3]^{2+}$, but the addition of each successive thienyl group had very little effect (3 nm shifts) with no significant changes in the respective excitation spectra. The emission profiles suggest that the emissive state is ^{3}MLCT Os(dπ) $\rightarrow \pi^*$ and that the π^* acceptor orbital is similar for each member of the series. This is consistent with the calculated finding that the LUMO is localized on the phen ligands and the phen portion of the IP ligands (Table 1 and Fig. S-29†). There was no evidence of an emissive ^{3}ILCT state.

Emission lifetimes were measured with a 355 nm laser pulse (pulse width $\approx$ 5 ns) excitation. The 2.1×10^2 ns lifetime of the series archetype $[Os(phen)_3]^{2+}$ in MeCN compared well to the literature lifetime in CH_2Cl_2 (315 ns)[67] and is shorter than that of the analogous $[Ru(phen)_3]^{2+}$ complex ($\tau \approx 500$ ns).[101,102] The similarity of the lifetimes ($\approx$200 ns) across the series further supports the conclusion that the ^{3}MLCT state involves the phen-based LUMO as the π^* acceptor in all the complexes. Complexes **Os-3T** and **Os-4T** also exhibited delayed emission ($\tau_2 = 3.8$–7.1×10^2 ns and 14–16 µs, respectively), which indicates that the ^{3}MLCT state can be populated from a state different than the initially-formed ^{1}MLCT state that leads to prompt ^{3}MLCT emission ($\tau_2 \approx 200$ ns). This proposed model is illustrated in the Jablonski diagram in Scheme 1. Given that the estimated ^{3}MLCT energy from emission measurements for **Os-4T** was about 1.66 eV and the computed value for the ^{3}ILCT state was 1.45 eV, we hypothesized that this energetic proximity could enable the longer-lived ^{3}ILCT state to act as an excited state energy reservoir for delayed ^{3}MLCT emission. This ^{3}MLCT–^{3}ILCT gap was estimated to be even smaller for **Os-3T**.

3.4.4 Transient absorption spectroscopy. The excited triplet states of the series were also examined using nanosecond transient absorption (TA) spectroscopy and analyzed in the context of related Ru(II) and Os(II) complexes.[103–105] The differential excited state absorption (ESA) spectra were measured in degassed (5× freeze–pump–thaw) MeCN with a 355 nm laser excitation pulse ($\approx$5 ns) and corrected for emission. The full relaxation spectra of the complexes are available in the ESI

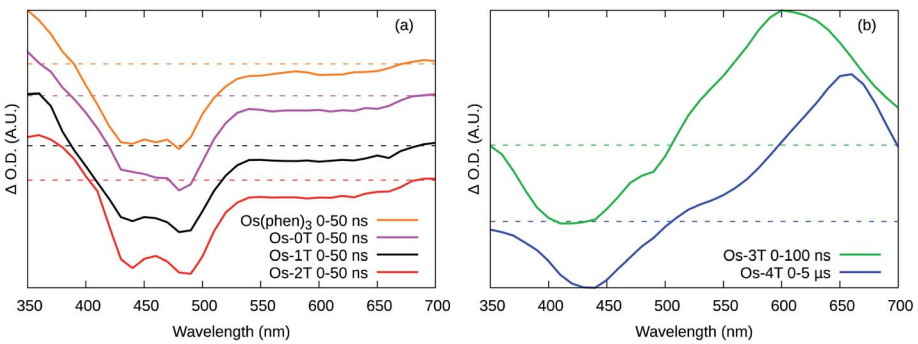

Fig. 8 Transient absorption profiles for (a) $[Os(phen)_3](PF_6)_2$, **Os-0T–Os-2T**, and (b) **Os-3T** and **Os-4T**, showing the indicated integration slices. $\Delta OD = 0$ is indicated by the dashed line of the corresponding color.

Table 6 Transient absorption lifetimes at selected wavelengths

Complex	Wavelength (nm)	τ_1 (ns)	τ_2 (ns)	τ_3 (ns)
$[Os(phen)_3]^{2+}$	360	2.2×10^2		
	440	2.1×10^2		
	480	2.1×10^2		
	600	2.0×10^2		
Os-0T	350	1.7×10^2		
	440	1.9×10^2		
	480	1.8×10^2		
	600	1.8×10^2		
Os-1T	360	1.6×10^2		
	440	1.6×10^2		
	480	1.7×10^2		
	600	1.8×10^2		
Os-2T	390	1.6×10^2		
	440	1.5×10^2	4.0×10^2	
	490	1.7×10^2	3.9×10^2	
	600	$1.5–1.7 \times 10^2$	$2.9–5.5 \times 10^2$	
Os-3T	430	$2.8–4.5 \times 10^2$	7.4×10^2	
	610	$3.6–4.8 \times 10^2$	7.1×10^2	
Os-4T	440	2.6×10^2	$3–4 \times 10^3$	12×10^3
	660	2.4×10^2	$3–4 \times 10^3$	$12–13 \times 10^3$

(Fig. S-37–S-43).† The TA and emission data were used to construct the Jablonski diagrams in Scheme 1.

The ESA spectra of $[Os(phen)_3](PF_6)_2$ and **Os-0T** through **Os-2T** (Fig. 8a) were qualitatively similar, featuring three regions. A strong bleach with peaks at around 440 and 480 nm corresponding to the loss of the ground state $^1A_1 \rightarrow$ MLCT transition. A broad, weaker bleach spanned ≈525–680 nm, also corresponding to loss of the MLCT transition. The absorption below 400 nm arises from a new excited state transition on the ^{3}MLCT radical anion ligand. The lifetimes were mono-exponential and essentially the same (≈150–200 ns) at all wavelengths for each compound (Table 6), indicating that the phen-based LUMO is involved in all these cases. The TA lifetimes also corresponded well with the emission lifetimes (Table 5), indicating that phosphorescent decay of the phen-based ^{3}MLCT state is the dominant relaxation pathway in these four compounds.

In contrast, **Os-3T** and **Os-4T** exhibited ESA spectra consistent with long-lived ligand-based triplet states (Fig. 8b) and which qualitatively resembled the spectra of the IP-*n*T ligands alone (Fig. S-44 and S-45†). The bleach in the 400–450 nm region corresponds to the loss of the strong ππ* transition, which peaks at around 413 nm and 436 nm in the ground state UV-vis absorbance spectra of the **Os-3T** and **Os-4T** complexes, respectively, and at 408 nm and 424 nm for the free IP-3T and IP-4T ligands. The broad and intense positive absorption in the ESA spectra of **Os-3T** and **Os-4T** was characteristic of transitions associated with one or more ligand-localized ^{3}ππ* states, which computational studies indicated were ^{3}ILCT in nature. These bands resembled those observed in the ESA spectra of the uncomplexed IP-3T and IP-4T ligands, indicating that the initially excited ^{1}ILCT and/or ^{1}MLCT states populate ^{3}ILCT states centered on the thiophene-containing ligand. The lack of this signature in the complexes with $n \leq 2$ suggests that this state is not energetically accessible and/or is not a dominant relaxation pathway in systems with less π-conjugated chains.

Os-0T and **Os-1T** displayed similar TA kinetics to $[Os(phen)_3](PF_6)_2$, with only one lifetime ($\tau_1 = 200$ ns) assigned as the emitting ^{3}MLCT state. This state was also observed for the other Os(II) complexes. The decay of the TA signal for **Os-2T** had an additional component (τ_2) that was slightly longer than τ_1 and not observed in the emission measurements. While this state could have ^{3}ILCT character, its contribution was weak (3–5% relative to τ_1) and the TA spectral signature for **Os-2T** was almost identical to the ^{3}MLCT signature of **Os-0T** and **Os-1T** (Fig. 8a).

The TA lifetimes of **Os-3T** and **Os-4T** were in agreement with their emission lifetimes and corroborated the model proposing delayed ^{3}MLCT emission through a second channel (Scheme 1). The TA kinetics of **Os-3T** were described by time constants of $\tau_1 < 500$ ns and $\tau_2 \approx 700$ ns, corresponding to the prompt and delayed kinetics observed in the emission measurements. The shorter component was assigned to prompt emission from the ^{3}MLCT state, while the longer component was assigned to the decay of an ^{3}ILCT state of similar energy *via* population of the emitting ^{3}MLCT state. The involvement of the ^{3}ILCT was invoked based on its computed energy being very similar to that of the ^{3}MLCT state and the characteristic signature of the ^{3}ILCT state observed in the TA spectrum that was absent from the complexes with fewer thiophene rings.

A similar model was invoked for **Os-4T**, which displayed three lifetimes in the TA measurements. The prompt decay ($\tau_1 \approx 250$ ns) was assigned to the emitting ^{3}MLCT state and agreed with the shorter component (τ_1) in the emission measurements. The longest TA lifetime ($\tau_3 \approx 12$ μs) agreed with the lifetime for delayed emission ($\tau_2 = 14–16$ μs) and was ascribed to the emitting ^{3}MLCT state populated from a lower-energy ^{3}ILCT state. The intermediate component ($\tau_2 \approx 3–4$ μs) was not

observed in the emission measurements and was assumed to be nonradiative decay of the dark ^{3}ILCT state back to the ground state. In this model, the ^{3}ILCT state has two discrete decay pathways whereby the longer lifetime could reflect the uphill process for ^{3}MLCT population due to the larger ^{3}MLCT-^{3}ILCT energy gap for **Os-4T** relative to **Os-3T** (Scheme 1).

3.5 Biological results

3.5.1 Cytotoxicity and photocytotoxicity toward cancer cells

3.5.1.1 Normoxic cellular assays. The dark and light cytotoxicities for $[Os(phen)_3]Cl_2$ through **Os-4T** were measured in SK-MEL-28 human skin melanoma cells growing as 2D adherent monolayers. Briefly, cells growing in log phase were seeded, dosed with compound (1 nM to 300 μM), and then incubated for 48 h before cell viability was determined using the resazurin viability assay for cytotoxicity. To determine photocytotoxicity, an analogous set of plates were prepared but were irradiated 15–22 h after compound addition. Dose–response curves were prepared from both dark and light conditions and analyzed to provide dark and light EC_{50} values, the effective concentration to reduce relative viability by 50%. PIs, or the light-induced amplification of cytotoxicity, were calculated as the ratios of the dark EC_{50} values to the light EC_{50} values. For highly potent compounds, the assay was adjusted to include a wider concentration range (10^{-12} to 300 μM). Any deviations from this method (hypoxia, different cell lines, *etc.*) are described as they are discussed. All of the complexes exhibited excellent solubility in high ionic strength solvents (DPBS, media) up to 50 μM, with $[Os(phen)_3]Cl_2$ as most soluble (>300 μM).

3.5.1.2 Dark cytotoxicity. The Os(II) oligothienyl complexes as well as reference compounds $[Os(phen)_3]Cl_2$ and **Os-0T** were relatively nontoxic toward SK-MEL-28 cells in the absence of a light treatment (Fig. 9a and Table S-4†), with dark EC_{50} values ranging from 158 to 35.7 μM. The least dark cytotoxic compound of the series was the reference compound $[Os(phen)_3]Cl_2$ (EC_{50} = 158 μM), and the most dark cytotoxic compound was **Os-2T** (EC_{50} = 35.7 μM). The dark cytotoxicities of **Os-1T**, **Os-3T**, and **Os-4T** (EC_{50} = 65.1 μM) were intermediate at 65–75 μM. These dark cytotoxicities did not correlate with the lipophilicities of the complexes, which increased with number of thienyl units. The reason behind the almost two-fold greater dark toxicity for **Os-2T**, with two thienyl groups, is unclear but agrees with our observations for other Os(II)- and Ru(II)-oligothiophene complexes (unpublished results).

3.5.1.3 Photocytotoxicity. The photocytotoxicities of the compounds in the series were assessed using a light fluence of 100 J cm^{-2} with broadband visible (400–700 nm, 21 mW cm^{-2}), green (523 nm, 18 mW cm^{-2}), and red (633 nm, 18 mW cm^{-2}) light. The spectral output of the light sources is shown in Fig. S-22 and S-23,† and the comparisons of the photocytotoxicity as EC_{50} values are shown in Fig. 9a.

The measured light EC_{50} values, which reflect contributions from both the dark and light cytotoxicity of each complex, generally increased with n in Fig. 9a and Table S-4.† The reference compound $[Os(phen)_3]Cl_2$ was considered relatively inactive, with visible EC_{50} values of 40–100 μM regardless of the light condition. The visible-light photocytotoxicities of the other compounds spanned almost six orders of magnitude. The values for compounds with n = 0–2 were in the 1–3 μM range, while that for **Os-3T** was nanomolar (EC_{50} = 153 nM). **Os-4T** was notable in its activity, with its visible EC_{50} value of 18 pM. These photocytotoxicities were attenuated slightly (but still within an order of magnitude) with the longer green (523 nm) and red (633 nm) wavelengths of light. However, the photocytotoxicity exerted by **Os-4T** exhibited a strong wavelength-dependence. Its 18 pM EC_{50} value fell to 1 nM with green light and 10 nM with red light. These EC_{50} values are still considered to be quite potent, but the wavelength dependence suggests a possible change in the mechanism with one mechanism clearly being more efficient than another.

3.5.1.4 Phototherapeutic index (PI). Because the photocytotoxicity, quantified as an EC_{50} value, contains contributions from any inherent dark cytotoxicity, the PI is the more appropriate benchmark for light-induced toxicity. The trends for the light EC_{50} values were reflected in the PIs that are compared in Fig. 9 and Table S-4.† Light had very little effect on the cytotoxicity of reference compound $[Os(phen)_3]Cl_2$ (PI = 2–4, regardless of wavelength). The PIs for compounds with n = 0–2 were larger than the reference compound, but still relatively low overall: <50 with visible light and near 10 or less for both green and red light. **Os-3T** had PI values that were generally ten-fold greater (PI_{vis} = 369, PI_{green} = 103, PI_{red} = 83) despite having a $^1O_2$ quantum yield (Φ_Δ = 51%) that was similar to that of $[Os(phen)_3]Cl_2$ and **Os-0T**–**Os-2T**. The spike in phototoxic effects for **Os-3T** is most likely due to the low-energy ^{3}ILCT state that becomes accessible at $n \geq 3$ as supported by computational studies and TA measurements.

Os-4T stood out among the series, not only with its near unity $^1O_2$ quantum yield and long triplet excited state lifetimes (3–4 μs and 14–16 μs), but also its exceptionally large PI_{vis} that exceeded 10^6. Even with attenuation at the lower-energy wavelengths, PIs were still >56 000 and >6500 with green and red light, respectively. McKenzie *et al.* have reported that a ratio of PI to light dose > 100 is rare.[107] In this respect, **Os-4T**'s visible and green PIs are among the largest in the literature and very intriguing.

Os-4T did have a much higher $^1O_2$ quantum yield (Φ_Δ = 95%) and the longest triplet excited state lifetime relative to the other compounds in the family. However, **Os-4T** is not unique in terms of its triplet state lifetime or its near unity $^1O_2$ quantum yield. Other complexes have such characteristics and even longer lifetimes.[23] It is also not particularly unusual in terms of its ground state absorption properties and ILCT triplet configuration; other complexes have similar profiles and exhibit less potency (*i.e.*, **Os-3T** as one example).[23] There were also no clear differences between compounds of the present family in terms of their computed excited state reactivities with oxygen or autoionization capacity, except that the complexes with $n \leq 2$ could directly form superoxide. The lower-energy ^{3}ILCT states in **Os-4T**, including the additional $\tau_2 \approx$ 3–4 μs process that was observed in the TA kinetics of **Os-4T** but absent for **Os-3T**, could be a starting point for better understanding this unique

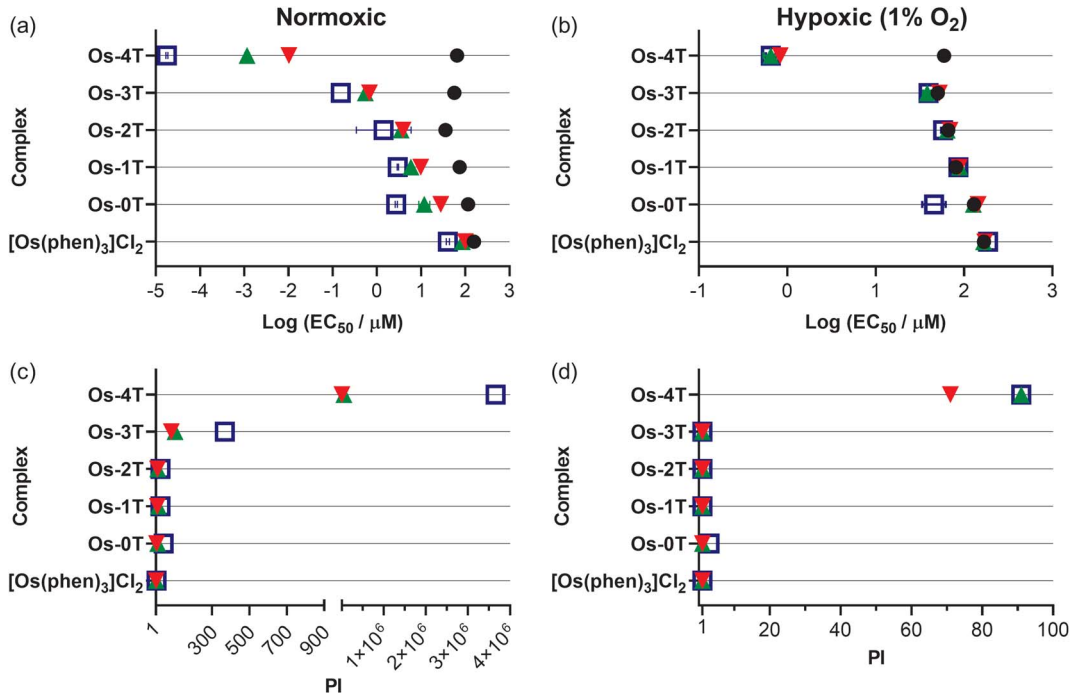

Fig. 9 Summary resazurin-based (photo)cytotoxicity of **Os-0T–Os-4T** compared to reference compound $[Os(phen)_3]Cl_2$ against SK-MEL-28 in normoxia (18.5–21% O_2;[106] left-column (a and c)) and hypoxia (1% O_2; right-column (b and d)). The phototherapeutic index (PI) as the ratio of light to dark cytotoxicity is plotted in (c) and (d). Figures are labelled as dark (no light; black circles) and 100 J cm^{-2} treatments at ~20 mW cm^{-2} as cool white visible (blue, open square), 523 nm (green, triangle) and 633 nm (red, inverted triangle). Results are tabulated in Tables S-4–S-7.†

compound. The pronounced wavelength-dependence for the activity of **Os-4T** may also support that initially populated ^{1}ILCT states are more efficient at producing the reactive triplets important for phototoxic effects.

3.5.1.5 Hypoxic cellular assays. The compounds were also assessed for their abilities to maintain a phototoxic response toward SK-MEL-28 cells under low oxygen conditions (hypoxia, 1% O_2). We have been investigating photobiological agents under hypoxic conditions, and have developed an optimized protocol for these difficult experiments.[41] Multiple parameters required optimization, including: incubation time in hypoxia prior to light treatment (DLI in hypoxia), the method for maintaining hypoxia during the light treatment (*e.g.*, low gas permeable films versus irradiating inside the hypoxia chamber), the post-PDT incubation period, and the cell viability determination protocol since metabolic viability indicators such as resazurin are strongly affected by hypoxic media. The reproducibility of this new protocol was evaluated over the past few years and found fairly robust with routine screens. The use of internal control(s) known to be strongly oxygen-dependent for their activity proved to be invaluable for experiment validation. Furthermore, passive gas exchange (surface-level) is only feasible to qualify hypoxic conditions if an appropriate time is allotted. We suggest that effective experiments to evaluate biological systems under hypoxia require either confirmation of (low) dissolved oxygen levels or sufficient measures to both control and maintain low oxygen at the point of light treatment. Without rigorous experimental design, studies may give misleading or irreproducible results. Unfortunately, this biases compounds to appear more promising than they truly are, distracting researchers from better agents or scaffolds remaining to be discovered.

These assays were run in parallel with normoxic assays (Fig. 9b and d) using our optimized hypoxia method[41] and included $[Ru(bpy)_2(dppn)]Cl_2$ as an O_2-dependent reference photosensitizer. Briefly, cells were equilibrated in hypoxia 2–3 h before treatment with the compounds and kept in hypoxia throughout the experiment (≥16 h). To mitigate any interference with the resazurin cell viability dye in hypoxia as we previously reported,[41] the samples were allowed to recover in normoxia after the light treatment. We have found post-irradiation recovery in normoxia to be a robust strategy for preserving the reliability of the resazurin indicator, confirmed by the absence of phototoxic effects for compounds that rely on oxygen for photocytotoxicity. The results are shown in Fig. 9 and tabulated in Table S-5.†

Almost all of compounds had dark EC_{50} values in hypoxia that were within about 10% of those in normoxia, with some compounds being slightly less dark toxic in hypoxia and others being slightly more. The exception was **Os-2T**, which showed a two-fold reduction in dark cytotoxicity in hypoxia. The photocytotoxicities of $[Os(phen)_3]Cl_2$ and **Os-0T–Os-3T** were very similar to their dark cytotoxicities, giving rise to PI values that were less than 2 in most cases and thus considered inactive as hypoxic phototoxic agents. **Os-4T**, again, was a notable exception. While its phototoxic effects were attenuated by several orders of magnitude, EC_{50} values were still submicromolar (651–835 nM) with $PI_{vis,green} = 91$ and $PI_{red} = 71$ (Table S-5†). A

striking observation was that the wavelength-dependence that was observed in normoxia (Fig. 9) was almost absent in hypoxia, suggesting that the photocytotoxicity in the two different oxygen conditions may derive from different excited states and/or pathways.

Since **Os-4T** stood out for its remarkable activity and because its activity in hypoxia was much larger than any we had previously published,[41] we used sulforhodamine B (SRB) as a secondary endpoint to confirm the activity determined with resazurin as the cell viability indicator. This additional endpoint confirmed the activity of **Os-4T** in hypoxia with total growth inhibition (TGI) values of 140–170 nM for light-treated samples (Tables S-6 and S-7†). The SRB quantification also revealed that the resazurin-interference observed previously for hypoxic experiments was not an issue for more potent compounds (defined as compounds with subnanomolar EC_{50} in the normoxic resazurin assay) such as **Os-4T**.

Clearly, there remains much work to be done in order to understand the potency observed for **Os-4T**. Before attempting a mechanistic understanding, we first wanted to validate and test the robustness of our findings (*e.g.*, reproducibility within our own lab and across different laboratories and researchers) and to explore the scope of this activity (*e.g.*, hypoxia, NIR, other cell lines).

3.5.1.6 In-house validation. To validate the photocytotoxicity we observed for **Os-4T**, we tested the reproducibility of this response in normoxia and hypoxia several months after the initial screen was conducted. The results are compiled in Fig. 10, Tables S-8 and S-9,† where 0 represents the initial data obtained for **Os-4T** from Fig. 9, and 1–5 are repeats of that experiment performed over a one-month period where certain factors were purposely varied: location of the various **Os-4T** concentrations on the microplate (by row), pipette tips used for serial dilution of the **Os-4T** stock solution, SK-MEL-28 seed stock batch, and room lighting. Consumables were of the same lot number and all cells were between 10–15 passages. Each repeat consisted of three replicates. In Fig. 10, hypoxic data points (1% O_2) are connected by dashed lines with open shapes and normoxic data points are connected by solid lines and solid shapes.

The dark cytotoxicity associated with **Os-4T** did not change substantially between the repeated experiments in either oxygen condition, with the average dark EC_{50} value being 62.8 μM with less than 7% variation. The photocytotoxicities and PIs for **Os-4T** showed variation across the repeated experiments compared to the dark cytotoxicity, but the variation was notably less than that for the normoxic condition. In hypoxia, the variation in phototoxic effects was relatively consistent across the three light conditions, with average EC_{50} values and PIs ranging from 351 nM to 1.80 μM and 32 to 167, respectively. The average hypoxic EC_{50} value and PI across the three light conditions were 0.816 μM and 90, respectively, with the exception of the repeat 3 (which was not included in the average because 1% O_2 was not maintained for that specific experiment).

The larger variation in normoxic photocytotoxicities and PIs also exhibited a wavelength dependence, with the most variation in the visible light condition (222%). The EC_{50} value ranges were greatest for the visible light treatment (0.0178 to 8.91 nM) and least for red (10.0 to 46.2 nM), with green being intermediate (1.16 to 25.4 nM). The values for PI_{vis} varied from 10^3 to 10^6, while values for PI_{red} were consistently $>10^3$ and PI_{green} ranged between 10^3 and 10^4. The average normoxic EC_{50} values for the visible, green, and red light treatments were 1.62 nM, 11.7 nM, and 30.8 nM, respectively. The corresponding average values for PI were on the order of 10^6, 10^4, and 10^3, respectively.

Together, the data indicates that the phototoxic mechanism that is operative in normoxia with shorter wavelengths of light is subject to a much greater degree of variability (three orders of magnitude) and different from the hypoxic phototoxic mechanism. Despite the variation, **Os-4T** remained extremely potent in normoxia even for the least potent repeat. Importantly, the hypoxic activity that we observed in the original set of experiments was confirmed across repeated screening and even the least potent repeats were still considered potent for hypoxia.

3.5.1.7 External validation. The family, excluding $[Os(phen)_3]Cl_2$, was further evaluated for their (photo)cytotoxicities in two cell lines in another laboratory by different researchers, whereby SK-MEL-28 was the human melanoma cell line used in-house (but not from the same seed stock) and the mouse B16-F10 melanoma cell line was an additional line. The assay was similar, including the light wavelengths and fluences employed, but the light sources and irradiances were different than those used to generate the data in Fig. 9.

While the Os(II) complexes were already relatively nontoxic to SK-MEL-28 cells in the absence of a light trigger, they were two-fold less dark toxic in the external validation experiments despite using similarly low cell passage numbers and had EC_{50} values that ranged from 123 to 238 μM (Fig. 11a and Table S-10†). The overall trend in photocytotoxicities followed the in-house trend, with potency increasing with the number of thiophenes rings in the chain. The PI_{vis} of **Os-4T** (Fig. 11b) was at the lower end of the range measured in-house at approximately 5×10^4 (visible $EC_{50} = 2.91$ nM), but its PI_{red} was ten-fold larger than in-house at 1.5×10^4 (red $EC_{50} = 9.44$ nM). In the case of shorter-wavelength visible light, the attenuated PI_{vis} externally measured could arise from the inherent variability already noted at the shorter wavelengths (Fig. 10) in combination with the different light source and higher irradiance used. For the larger PI_{red} measured externally, the discrepancy could be due to different light sources and irradiances having been used and that the external SK-MEL-28 cells were more dark-resistant compared to those that were used in-house.

To test the robustness of this response toward melanoma cells, the external validation study also compared the activities of the compounds toward a highly pigmented murine B16-F10 cell line since melanoma cells can vary widely in pigmentation[108] and pigmentation can reduce phototoxic effects.[109,110] The compounds were also relatively nontoxic to the highly pigmented murine B16-F10 cell line in the dark (Fig. 11c and Table S-10†). Their dark EC_{50} values were 140–190 μM and 300 μM for **Os-0T–Os-3T** and **Os-4T**, respectively. **Os-3T** and **Os-4T**

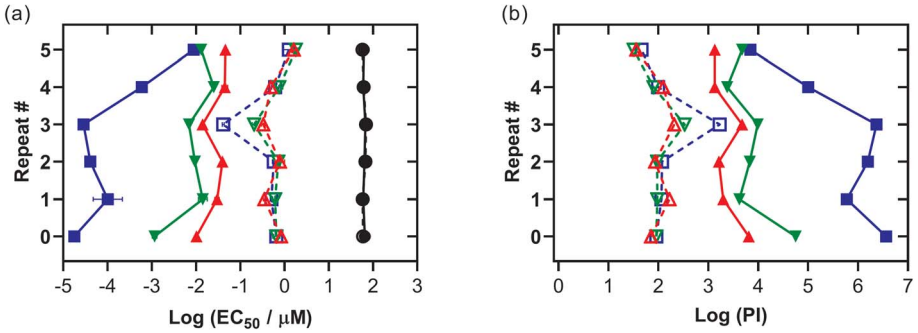

Fig. 10 Summary of **Os-4T** interassay performance in SK-MEL-28 with various factors changed across each repeat as described in the experimental. Normoxic points are connected by solid lines and labelled as dark (no light; black circles) and 100 J cm^{-2} treatments at ~20 mW cm^{-2} as cool white visible (blue, square), 523 nm (green, inverted triangle) and 633 nm (red, triangle) ± log(SEM). SEM = standard error of the mean. Hypoxic treated plates (1% O_2) are connected by dashed lines and open shapes for the same color scheme.

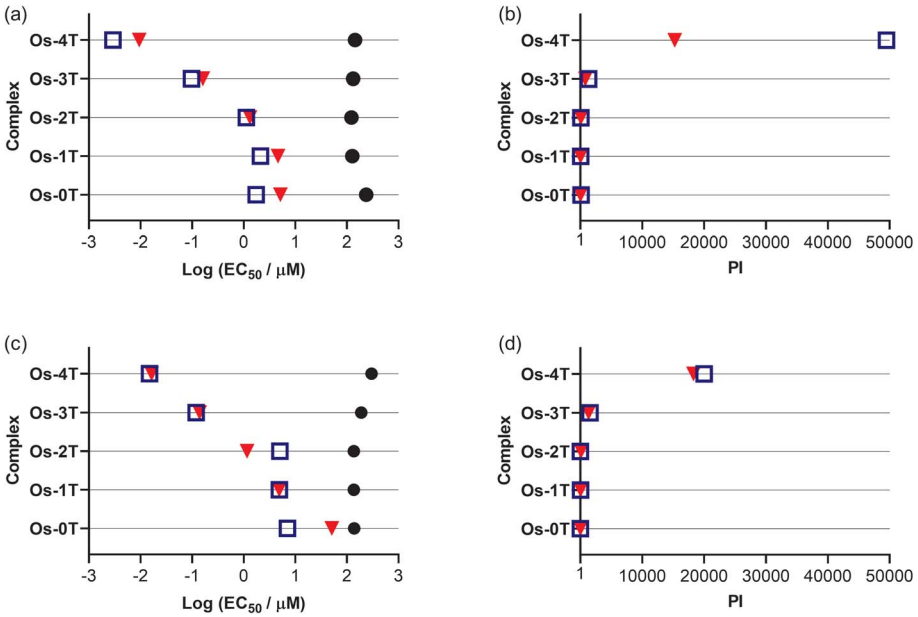

Fig. 11 Summary resazurin-based (photo)cytotoxicity of **Os-0T**–**Os-4T** in normoxia against human amelanotic SK-MEL-28 (a and b) and murine melanotic B16-F10 (c and d) cell lines. Figures are labelled as dark (no light; black circles) and 100 J cm^{-2} treatments using 33 mW cm^{-2} visible (blue, open square) or 40 mW cm^{-2} 633 nm (red, inverted triangle).

were less dark toxic toward the B16-F10 cell line relative to the SK-MEL-28 line.

Their photocytotoxicity trends with increasing *n* paralleled those in SK-MEL-28 (external validation), with nanomolar activity for **Os-3T** and **Os-4T** (Fig. 11c and d). However, their visible EC_{50} values were larger across the series compared to SK-MEL-28 and indicated greater resistance to visible light-induced toxicity in the B16-F10 cell line, where EC_{50} values ranged from 15 nM for **Os-4T** to 7.04 μM for **Os-0T**. Only **Os-0T** and **Os-4T** were attenuated with red light in B16-F10 with respect to red EC_{50} values in the SK-MEL-28 cell line: ten-fold for **Os-0T** and two-fold for **Os-4T**. Despite this attenuation, **Os-3T** and **Os-4T** had similar PI values as those measured in the SK-MEL-28 cell line for both light conditions due to their lower dark cytotoxicity toward the murine B16-F10 cell line. For **Os-4T**, the visible and red PIs were still >20 000 and >18 000, respectively and were comparable to those measured externally for the SK-MEL-28 cell line. The absence of a difference in photocytotoxicity between the visible and red light treatments in the B16-F10 cell line for **Os-4T**, which was observed for SK-MEL-28 (both in-house and externally), may reflect the ability of increased melanin (from more advanced melanosome stages)[108] in the highly pigmented B16-F10 cells to absorb the shorter wavelengths.

3.5.1.8 Fluence and irradiance. The scope of photoactivity toward the SK-MEL-28 cell line was explored further for **Os-4T** using monochromatic laser light with a smaller bandwidth rather than LEDs, with the opportunity to precisely deliver various fluence and irradiance combinations well-by-well (37 °C, 5% CO_2) using the Modulight ML8500 platform. The response as a function of light fluence was explored at two

different concentrations (0.5 and 1.0 μM) and wavelengths (525 and 630 nm; Fig. 12a and b). Higher concentrations combined with larger fluences yielded greater potency following what would be expected for PDT dosing (μM J cm^{-2}). Green light was more effective than red light at lower fluences for the two concentrations tested, but the two wavelengths both yielded maximal and indistinguishable potency around 100 J cm^{-2} and higher. The irradiance dependence in Fig. 12c and d was explored using a fluence of 100 J cm^{-2} and 525 nm light (100 nM) or 630 nm light (250 nM), which were conditions where the Modulight illumination system gave sub-maximal potency. In this region, we were able to observe that lower irradiances yielded higher photocytotoxicity and that the higher concentration used for the red-light condition was more susceptible. In other words, the phototoxicity with red light can be improved at a defined fluence by lowering the irradiance and increasing the concentration of **Os-4T**. This flexibility is advantageous when progressing to *in vivo* models.

3.5.1.9 Near-infrared (NIR) activation. We also investigated the photocytotoxicity of **Os-4T** toward SK-MEL-28 cells using wavelengths in the so-called PDT window (700–900 nm) despite minimal absorption in this region. Only high concentrations (≥10 μM) combined with very high fluences (≥400 J cm^{-2}) yielded a marginal response (14% viability reduction) with 753 nm delivered at an irradiance of 300 mW cm^{-2} (Fig. S-46†). However, shortening the excitation by only 20 nm produced a substantial change in the NIR response of **Os-4T**. When 733 nm light was delivered at low irradiance (5 mW cm^{-2}), we observed submicromolar response with EC_{50} = 0.803 μM and a $PI_{733\ nm}$ of 77 with 100 J cm^{-2} fluence (Fig. 13). This was the same fluence (albeit at lower irradiance) used in the dose–response data plotted in Fig. 9, where the molar extinction coefficient at 733 nm for **Os-4T** was less than 300 M^{-1} cm^{-1}.

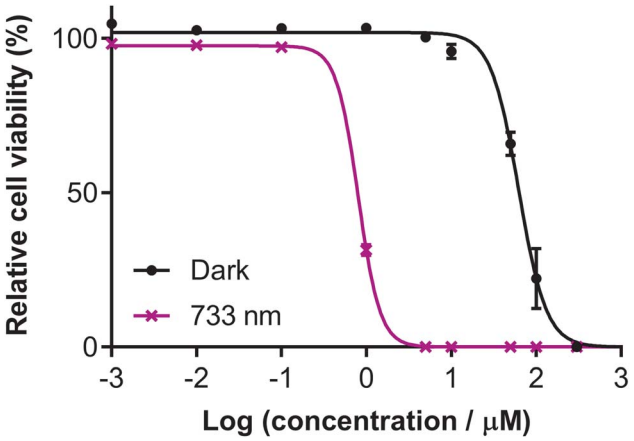

Fig. 13 Dose–response (±SD) of **Os-4T** in SK-MEL-28 cells with 733 nm light at 100 J cm^{-2} and 5 mW cm^{-2}. Dark (sham) treatments are black filled circles and 733 nm violet crosses.

This NIR photocytotoxicity was sensitive to oxygen tension and disappeared in hypoxia (1% O_2, $PI_{733\ nm}$ = 1).

3.5.1.10 Maximum tolerated dose (MTD) in mice. Since our *in vitro* models indicated low dark toxicity (and even lower in the murine line), maximum tolerated dose (MTD) studies were performed on female C57BL/6J mice to gauge whether *in vivo* phototoxicity experiments were a logical next step. The mice treated by intraperitoneal injection of **Os-4T** were observed to experience mild toxicity at doses above 100 mg kg^{-1}. At the three tested doses of 100, 125, and 200 mg kg^{-1}—all animals displayed signs of stress (intermittent hunching, ears laid back), were subdued but responsive, and experienced weight loss. Their irregular behavior, however, resolved after 2 h. Since no signs of moderate toxicity were detected over the 2 week study, the intraperitoneal MTD of **Os-4T** was determined to be

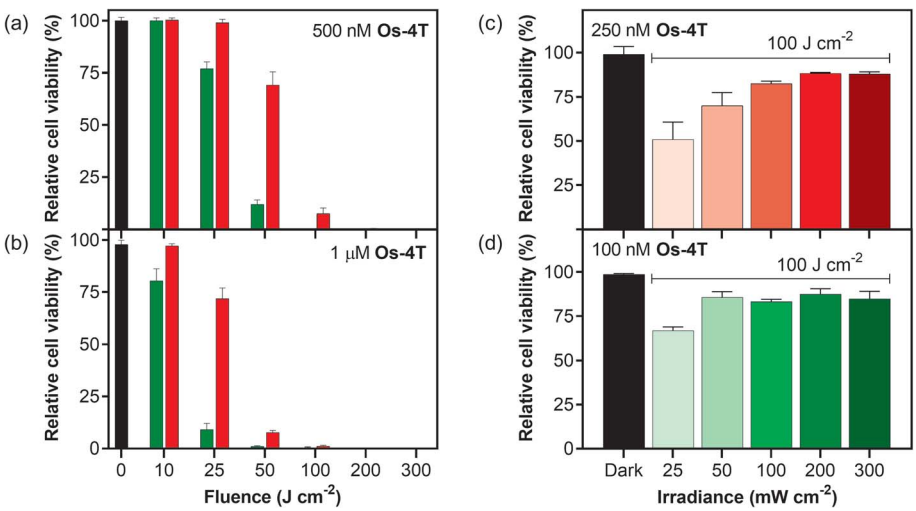

Fig. 12 Dosimetry experiments on the Modulight ML8500 (37 °C, 5% CO_2) in triplicate (±SD) with viability based on resazurin. Fluence dependence of (a) 500 nM or (b) 1 μM **Os-4T** against SK-MEL-28 at 300 mW cm^{-2}. The left-most column is a dark (no-light; black bar) reference of compound cytotoxicity. Light treatments included 10–300 J cm^{-2} of either 525 nm (left bar, green) or 630 nm (right bar, red). Irradiance dependence of **Os-4T** with either no light (left, dark, black bar), (c) 630 nm and 250 nM, or (d) 525 nm and 100 nM treatments at 100 J cm^{-2} and 25–300 mW cm^{-2}.

≥200 mg kg^{-1}. Since the complex **Os-4T** is highly phototoxic in normoxia, active in hypoxia, active in the photodynamic window at 733 nm, and nontoxic in mice, we plan to investigate this compound for its *in vivo* light-triggered antitumor properties.

4. Conclusions

This study highlights the structure–activity relationships for a series of $[Os(phen)_2(IP\text{-}nT)]Cl_2$ complexes from $n = 0$ to 4 with respect to ground and excited state geometries and configurations, $^1O_2$ quantum yields, excited state lifetimes, and dark and light cytotoxicities toward melanoma cells in normoxia and hypoxia using various light parameters. Our hypothesis was that an abrupt switch in photophysical behavior would occur at some critical *n*, where a lowest energy ^{3}ILCT state would dominate the excited state dynamics and lead to increased sensitivity to oxygen that might be maintained even in hypoxia. This strategy was applied successfully for the analogous Ru(II) series and resulted in TLD1433, which is the first non-tetrapyrrole-based metal complex to enter human clinical trials for treating cancer with PDT. Replacement of Ru(II) with the heavier Os(II) center serves to shift the optical window for activation to longer wavelengths with higher quantum yields for triplet state formation for all of the complexes, while keeping the highly reactive ^{3}ILCT state at the requisite energy for potent phototoxicity only for certain values of *n*.

The computational studies corroborated the critical point ($n \geq 3$) for switching to a lowest lying ^{3}ILCT state as determined by TA spectroscopy and did suggest that the ^{3}ILCT state for **Os-4T** would be better positioned energetically to dominate the photophysics, but did not explain the unusual reactivity of **Os-4T**. While the high $^1O_2$ quantum yield and prolonged lifetime for **Os-4T** could explain why this compound stood out among the series, these factors cannot be solely responsible for the picomolar potency and PI > 10^6 with visible light. An interesting facet to its activity was that the photocytotoxic response with visible light (enriched in the shorter, bluer wavelengths) varied by over three orders of magnitude with repeated experiments in normoxia, but even at its least potent was nanomolar with PIs >10^4. Even at its least potent, it still has one of the largest PIs reported. This potency was attenuated with the longer green and red wavelengths of light, but was not subject to the large variation in response observed with the shorter wavelengths. These results seem to point toward a different mechanism of action for the phototoxic effect with visible light. Interestingly, there was no drastic variation in the visible light response in hypoxia, and there was also almost no difference in the potencies between the shorter and longer wavelengths in hypoxia. This observation points toward a different phototoxic mechanism in hypoxia (at least with visible light) compared to normoxia.

While we are currently investigating the mechanism, we felt it more urgent to confirm our potency in an additional melanoma cell line and by other researchers given that results can be highly variable between laboratories running cytotoxic assays, especially with the added complexity of the light treatment (different light sources, wavelengths, fluences, irradiances, *etc.*). While the PI of **Os-4T** with visible light in normoxia measured externally was at the lower end of the range we measured in-house (but still low nanomolar with a PI > 10^4), the red PI was ten-fold higher. In the highly pigmented mouse melanoma cells, these PIs were attenuated but still >10^4.

The photocytotoxicity of **Os-4T** demonstrated an irradiance dependence, where larger PIs were obtained with lower irradiance. This afforded the opportunity to optimize the light parameters to achieve a response with NIR light at 733 nm, where the EC_{50} value was still submicromolar with a PI of almost 10^2. Given this versatility and robustness in response combined with its high aqueous solubility, we examined the MTD in mice and found that **Os-4T** was tolerated very well (MTD > 200 mg kg^{-1} by intraperitoneal injection). As we demonstrated for our previous Os(II) panchromatic absorbers in an *in vivo* investigation, **Os-4T** is yet another example that dispels the myth that Os (regardless of oxidation state) is an inherently toxic metal that cannot be used in medicine

The unprecedented photoactivities observed for **Os-4T** will certainly be explored using more sophisticated models in future work. In addition, next steps are aimed at delineating the mechanism of action across the different wavelengths and oxygen concentrations, which would lay the foundation for increasing activities in hypoxia and with NIR wavelengths of light while developing our understanding of the photophysical relationship to photocytotoxicity in compounds of this class.

Conflicts of interest

S. A. M. has a potential research conflict of interest due to a financial interest with Theralase Technologies, Inc. and PhotoDynamic, Inc. A management plan has been created to preserve objectivity in research in accordance with UTA policy.

Acknowledgements

S. A. M., C. G. C., and G. D. thank the National Cancer Institute (NCI) of the National Institutes of Health (NIH) (Award R01CA222227) for partial support of this work. The content is solely the responsibility of the authors and does not necessarily represent the official views of the National Institutes of Health. S. A. M. also acknowledges the Canadian Institutes of Health Research (CIHR), the Natural Sciences and Engineering Council of Canada (NSERC), the Canadian Foundation for Innovation (CFI), and the Nova Scotia Research and Innovation Trust (NSRIT) for support. S. A. M. would also like to thank Prof. Edith (Phoebe) Glazer for insightful discussions. N. R. and M. E. A. are grateful to the Università della Calabria. M. E. A. would also like to thank Dr Antonio Francés Monerris for the valuable and constructive discussion. S. A. M. also thanks Dr Daniel Todd as UNCG's Triad Mass Spectrometry Facility manager and his assistants Jennifer Simpson and Diane Wallace. We thank Dr Franklin Moy for his experimental support and instrument maintenance as UNCG's NMR facility manager.

References

1 World Health Organization, *World health statistics 2019: monitoring health for the SDGs, sustainable development goals.*, World Health Organization, S.l., 2019.
2 *Prodrugs: challenges and rewards*, ed. V. J. Stella, Springer: AAPS Press, New York, NY, 2007.
3 F. Kratz, I. A. Müller, C. Ryppa and A. Warnecke, *ChemMedChem*, 2008, **3**, 20–53.
4 I. Giang, E. L. Boland and G. M. K. Poon, *AAPS J.*, 2014, **16**, 899–913.
5 R. S. Kerbel, H. Kobayashi and C. H. Graham, *J. Cell. Biochem.*, 1994, **56**, 37–47.
6 A. Sharma, *Nanomed*, 2017, **12**, 2137–2148.
7 E. C. Fiedler and M. T. Hemann, *Annu. Rev. Cancer Biol.*, 2019, **3**, 409–428.
8 A. S. Azmi, B. Bao and F. H. Sarkar, *Cancer Metastasis Rev.*, 2013, **32**, 623–642.
9 E. B. Rankin and A. J. Giaccia, *Science*, 2016, **352**, 175–180.
10 L. Vera-Ramirez and K. W. Hunter, *F1000Research*, 2017, **6**, 2134.
11 *Photodynamic therapy: basic principles and clinical applications*, ed. B. W. Henderson and T. J. Dougherty, Dekker, New York, 1992.
12 T. J. Dougherty, C. J. Gomer, B. W. Henderson, G. Jori, D. Kessel, M. Korbelik, J. Moan and Q. Peng, *J. Natl. Cancer Inst.*, 1998, **90**, 889–905.
13 R. Bonnett, *Chemical aspects of photodynamic therapy*, Gordon and Breach Science Publishers, Amsterdam, The Netherlands, 2000.
14 *Advances in photodynamic therapy: basic, translational, and clinical*, ed. M. R. Hamblin and P. Mróz, Artech House, Boston, Mass, 2008.
15 K. Plaetzer, B. Krammer, J. Berlanda, F. Berr and T. Kiesslich, *Lasers Med. Sci.*, 2009, **24**, 259–268.
16 P. Agostinis, K. Berg, K. A. Cengel, T. H. Foster, A. W. Girotti, S. O. Gollnick, S. M. Hahn, M. R. Hamblin, A. Juzeniene, D. Kessel, M. Korbelik, J. Moan, P. Mroz, D. Nowis, J. Piette, B. C. Wilson and J. Golab, *Ca-Cancer J. Clin.*, 2011, **61**, 250–281.
17 *Handbook of photomedicine*, ed. M. R. Hamblin and Y.-Y. Huang, CRC Press, Boca Raton, FL, 2014.
18 R. R. Allison, *Future Oncol.*, 2014, **10**, 123–124.
19 L. Benov, *Med. Princ. Pract.*, 2015, **24**, 14–28.
20 *Photodynamic medicine: from bench to clinic*, ed. H. Kostron, T. Hasan and Royal Society of Chemistry (Great Britain), Royal Society of Chemistry, Cambridge, 2016.
21 H. Abrahamse and M. R. Hamblin, *Biochem. J.*, 2016, **473**, 347–364.
22 D. van Straten, V. Mashayekhi, H. de Bruijn, S. Oliveira and D. Robinson, *Cancers*, 2017, **9**, 19.
23 S. Monro, K. L. Colón, H. Yin, J. Roque, P. Konda, S. Gujar, R. P. Thummel, L. Lilge, C. G. Cameron and S. A. McFarland, *Chem. Rev.*, 2019, **119**, 797–828.
24 B. Q. Spring, I. Rizvi, N. Xu and T. Hasan, *Photochem. Photobiol. Sci.*, 2015, **14**, 1476–1491.
25 T. Minervini, B. Cardey, S. Foley, C. Ramseyer and M. Enescu, *Metallomics*, 2019, **11**, 833–844.
26 T. Respondek, R. N. Garner, M. K. Herroon, I. Podgorski, C. Turro and J. J. Kodanko, *J. Am. Chem. Soc.*, 2011, **133**, 17164–17167.
27 B. S. Howerton, D. K. Heidary and E. C. Glazer, *J. Am. Chem. Soc.*, 2012, **134**, 8324–8327.
28 E. C. Glazer, *Isr. J. Chem.*, 2013, **53**, 391–400.
29 E. Wachter and E. C. Glazer, *J. Phys. Chem. A*, 2014, **118**, 10474–10486.
30 A. Bahreman, J.-A. Cuello-Garibo and S. Bonnet, *Dalton Trans.*, 2014, **43**, 4494–4505.
31 J. D. Knoll, B. A. Albani and C. Turro, *Acc. Chem. Res.*, 2015, **48**, 2280–2287.
32 T. Sainuddin, M. Pinto, H. Yin, M. Hetu, J. Colpitts and S. A. McFarland, *J. Inorg. Biochem.*, 2016, **158**, 45–54.
33 J.-A. Cuello-Garibo, M. S. Meijer and S. Bonnet, *Chem. Commun.*, 2017, **53**, 6768–6771.
34 J.-A. Cuello-Garibo, E. Pérez-Gallent, L. van der Boon, M. A. Siegler and S. Bonnet, *Inorg. Chem.*, 2017, **56**, 4818–4828.
35 J. K. White, R. H. Schmehl and C. Turro, *Inorg. Chim. Acta*, 2017, **454**, 7–20.
36 S. Bonnet, *Dalton Trans.*, 2018, **47**, 10330–10343.
37 M. H. Al-Afyouni, T. N. Rohrabaugh, K. F. Al-Afyouni and C. Turro, *Chem. Sci.*, 2018, **9**, 6711–6720.
38 A. Li, C. Turro and J. J. Kodanko, *Chem. Commun.*, 2018, **54**, 1280–1290.
39 D. Havrylyuk, M. Deshpande, S. Parkin and E. C. Glazer, *Chem. Commun.*, 2018, **54**, 12487–12490.
40 D. Havrylyuk, K. Stevens, S. Parkin and E. C. Glazer, *Inorg. Chem.*, 2020, **59**, 1006–1013.
41 J. Roque, D. Havrylyuk, P. C. Barrett, T. Sainuddin, J. McCain, K. Colón, W. T. Sparks, E. Bradner, S. Monro, D. Heidary, C. G. Cameron, E. C. Glazer and S. A. McFarland, *Photochem. Photobiol.*, 2020, **96**, 327–339.
42 A. Juris, V. Balzani, F. Barigelletti, S. Campagna, P. Belser and A. von Zelewsky, *Coord. Chem. Rev.*, 1988, **84**, 85–277.
43 K. Kalyanasundaram, *Photochemistry of polypyridine and porphyrin complexes*, Acad. Pr., London, 1992.
44 V. Balzani, A. Juris, M. Venturi, S. Campagna and S. Serroni, *Chem. Rev.*, 1996, **96**, 759–834.
45 V. Balzani, A. Credi and M. Venturi, *Coord. Chem. Rev.*, 1998, **171**, 3–16.
46 V. Balzani and A. Juris, *Coord. Chem. Rev.*, 2001, **211**, 97–115.
47 S. Campagna, F. Puntoriero, F. Nastasi, G. Bergamini and V. Balzani, in *Photochemistry and Photophysics of Coordination Compounds I*, ed. V. Balzani and S. Campagna, Springer Berlin Heidelberg, Berlin, Heidelberg, 2007, vol. 280, pp. 117–214.
48 C. L. Evans, A. O. Abu-Yousif, Y. J. Park, O. J. Klein, J. P. Celli, I. Rizvi, X. Zheng and T. Hasan, *PLoS One*, 2011, **6**, e23434.
49 W. Feng, C. Gao, W. Liu, H. Ren, C. Wang, K. Ge, S. Li, G. Zhou, H. Li, S. Wang, G. Jia, Z. Li and J. Zhang, *Chem. Commun.*, 2016, **52**, 9434–9437.

50 L. N. Lameijer, D. Ernst, S. L. Hopkins, M. S. Meijer, S. H. C. Askes, S. E. Le Dévédec and S. Bonnet, *Angew. Chem., Int. Ed.*, 2017, **56**, 11549–11553.
51 Z. Lv, H. Wei, Q. Li, X. Su, S. Liu, K. Y. Zhang, W. Lv, Q. Zhao, X. Li and W. Huang, *Chem. Sci.*, 2018, **9**, 502–512.
52 V. H. S. van Rixel, V. Ramu, A. B. Auyeung, N. Beztsinna, D. Y. Leger, L. N. Lameijer, S. T. Hilt, S. E. Le Dévédec, T. Yildiz, T. Betancourt, M. B. Gildner, T. W. Hudnall, V. Sol, B. Liagre, A. Kornienko and S. Bonnet, *J. Am. Chem. Soc.*, 2019, **141**, 18444–18454.
53 Q. Yu, T. Huang, C. Liu, M. Zhao, M. Xie, G. Li, S. Liu, W. Huang and Q. Zhao, *Chem. Sci.*, 2019, **10**, 9091–9098.
54 V. Novohradsky, A. Rovira, C. Hally, A. Galindo, G. Vigueras, A. Gandioso, M. Svitelova, R. Bresolí-Obach, H. Kostrhunova, L. Markova, J. Kasparkova, S. Nonell, J. Ruiz, V. Brabec and V. Marchán, *Angew. Chem., Int. Ed.*, 2019, **58**, 6311–6315.
55 M.-D. Li, N.-K. Wong, J. Xiao, R. Zhu, L. Wu, S.-Y. Dai, F. Chen, G. Huang, L. Xu, X. Bai, M. R. Geraskina, A. H. Winter, X. Chen, Y. Liu, W. Fang, D. Yang and D. L. Phillips, *J. Am. Chem. Soc.*, 2018, **140**, 15957–15968.
56 A. Li, R. Yadav, J. K. White, M. K. Herroon, B. P. Callahan, I. Podgorski, C. Turro, E. E. Scott and J. J. Kodanko, *Chem. Commun.*, 2017, **53**, 3673–3676.
57 G. Shi, S. Monro, R. Hennigar, J. Colpitts, J. Fong, K. Kasimova, H. Yin, R. DeCoste, C. Spencer, L. Chamberlain, A. Mandel, L. Lilge and S. A. McFarland, *Coord. Chem. Rev.*, 2015, **282–283**, 127–138.
58 E. M. Kober, J. V. Caspar, B. P. Sullivan and T. J. Meyer, *Inorg. Chem.*, 1988, **27**, 4587–4598.
59 *Photochemistry and photophysics of coordination compounds. 1*, ed. G. Accorsi and V. Balzani, Springer, Berlin, 2007.
60 *Photodynamic therapy: From Theory to Application*, ed. M. Abdel-Kadel, Springer, New York, 2013.
61 G. E. Shillito, C. B. Larsen, J. R. W. McLay, N. T. Lucas and K. C. Gordon, *Inorg. Chem.*, 2016, **55**, 11170–11184.
62 S. Lazic, P. Kaspler, G. Shi, S. Monro, T. Sainuddin, S. Forward, K. Kasimova, R. Hennigar, A. Mandel, S. McFarland and L. Lilge, *Photochem. Photobiol.*, 2017, **93**, 1248–1258.
63 E. C. Glazer, *Photochem. Photobiol.*, 2017, **93**, 1326–1328.
64 Z. Wang, in *Comprehensive Organic Name Reactions and Reagentsang*, 2010, vol. 3.
65 G. Ghosh, K. L. Colón, A. Fuller, T. Sainuddin, E. Bradner, J. McCain, S. M. A. Monro, H. Yin, M. W. Hetu, C. G. Cameron and S. A. McFarland, *Inorg. Chem.*, 2018, **57**, 7694–7712.
66 L. Pazderski, T. Pawlak, J. Sitkowski, L. Kozerski and E. Szłyk, *Magn. Reson. Chem.*, 2010, **48**, 450–457.
67 W. J. Vining, J. V. Caspar and T. J. Meyer, *J. Phys. Chem.*, 1985, **89**, 1095–1099.
68 M. J. Frisch, G. W. Trucks, H. B. Schlegel, G. E. Scuseria, M. A. Robb, J. R. Cheeseman, G. Scalmani, V. Barone, B. Mennucci, G. A. Petersson, H. Nakatsuji, M. Caricato, X. Li, H. P. Hratchian, A. F. Izmaylov, J. Bloino, G. Zheng, J. L. Sonnenberg, M. Hada, M. Ehara, K. Toyota, R. Fukuda, J. Hasegawa, M. Ishida, T. Nakajima, Y. Honda, O. Kitao, H. Nakai, T. Vreven, J. A. Montgomery Jr, J. E. Peralta, F. Ogliaro, M. Bearpark, J. J. Heyd, E. Brothers, K. N. Kudin, V. N. Staroverov, R. Kobayashi, J. Normand, K. Raghavachari, A. Rendell, J. C. Burant, S. S. Iyengar, J. Tomasi, M. Cossi, N. Rega, J. M. Millam, M. Klene, J. E. Knox, J. B. Cross, V. Bakken, C. Adamo, J. Jaramillo, R. Gomperts, R. E. Stratmann, O. Yazyev, A. J. Austin, R. Cammi, C. Pomelli, J. W. Ochterski, R. L. Martin, K. Morokuma, V. G. Zakrzewski, G. A. Voth, P. Salvador, J. J. Dannenberg, S. Dapprich, A. D. Daniels, Ö. Farkas, J. B. Foresman, J. V. Ortiz, J. Cioslowski and D. J. Fox, *Gaussian09*, Gaussian, Inc., Wallingford, CT, 2009.
69 M. E. Casida, in *Recent developments and applications of modern density functional theory*, ed. J. M. Seminario, Elsevier, Amsterdam, Netherlands, 1996, pp. 155–192.
70 C. Adamo and V. Barone, *J. Chem. Phys.*, 1999, **110**, 6158–6170.
71 M. Cossi and V. Barone, *J. Chem. Phys.*, 2000, **112**, 2427–2435.
72 J. Tomasi, B. Mennucci and R. Cammi, *Chem. Rev.*, 2005, **105**, 2999–3094.
73 D. Andrae, U. Häußermann, M. Dolg, H. Stoll and H. Preuß, *Theor. Chim. Acta*, 1990, **77**, 123–141.
74 Y. Zhao and D. G. Truhlar, *Theor. Chem. Acc.*, 2008, **120**, 215–241.
75 (*a*) C. Latouche, D. Skouteris, F. Palazzetti and V. Barone, *J. Chem. Theory Comput.*, 2015, **11**, 3281–3289; (*b*) M. E. Alberto and C. Adamo, *Chem.–Eur. J.*, 2017, **23**, 15124–15132.
76 M. E. Alberto, J. Pirillo, N. Russo and C. Adamo, *Inorg. Chem.*, 2016, **55**, 11185–11192.
77 M. DeRosa, *Coord. Chem. Rev.*, 2002, **233–234**, 351–371.
78 P. Skehan, R. Storeng, D. Scudiero, A. Monks, J. McMahon, D. Vistica, J. T. Warren, H. Bokesch, S. Kenney and M. R. Boyd, *J. Natl. Cancer Inst.*, 1990, **82**, 1107–1112.
79 V. Vichai and K. Kirtikara, *Nat. Protoc.*, 2006, **1**, 1112–1116.
80 J. Blois, A. Smith and L. Josephson, *Cancer Chemother. Pharmacol.*, 2011, **68**, 795–803.
81 R. H. Shoemaker, *Nat. Rev. Cancer*, 2006, **6**, 813–823.
82 Y. Arenas, S. Monro, G. Shi, A. Mandel, S. McFarland and L. Lilge, *Photodiagn. Photodyn. Ther.*, 2013, **10**, 615–625.
83 S. A. McFarland, Metal-based Thiophene Photodynamic Compounds and Their Use, *US Pat.*, number 9,345,769, issued May 24, 2016.
84 S. A. McFarland, Metal-based Thiophene Photodynamic Compounds and Their Use, *US Pat.*, number 9,676,806 B2, issued June 13, 2017.
85 L.-F. Tan, F. Wang, H. Chao, Y.-F. Zhou and C. Weng, *J. Inorg. Biochem.*, 2007, **101**, 700–708.
86 H. Xu, K.-C. Zheng, L.-J. Lin, H. Li, Y. Gao and L.-N. Ji, *J. Inorg. Biochem.*, 2004, **98**, 87–97.
87 Q.-X. Zhen, B.-H. Ye, J.-G. Liu, Q.-L. Zhang, L.-N. Ji and L. Wang, *Inorg. Chim. Acta*, 2000, **303**, 141–147.
88 J.-Z. Wu and L.-N. Ji, *Transition Met. Chem.*, 1999, **24**, 299–303.
89 C.-W. Jiang, H. Chao, R.-H. Li, H. Li and L.-N. Ji, *Polyhedron*, 2001, **20**, 2187–2193.

90 R. A. Scherrer and S. M. Howard, *J. Med. Chem.*, 1977, **20**, 53–58.
91 G. Lanzani, M. Nisoli, S. De Silvestri and R. Tubino, *Chem. Phys. Lett.*, 1996, **251**, 339–345.
92 J.-P. Yang, W. Paa and S. Rentsch, *Chem. Phys. Lett.*, 2000, **320**, 665–672.
93 Y. Arenas, S. Monro, G. Shi, A. Mandel, S. McFarland and L. Lilge, *Photodiagn. Photodyn. Ther.*, 2013, **10**, 615–625.
94 P. Kaspler, S. Lazic, S. Forward, Y. Arenas, A. Mandel and L. Lilge, *Photochem. Photobiol. Sci.*, 2016, **15**, 481–495.
95 M. E. Alberto, B. C. De Simone, G. Mazzone, E. Sicilia and N. Russo, *Phys. Chem. Chem. Phys.*, 2015, **17**, 23595–23601.
96 J. Llano, J. Raber and L. A. Eriksson, *J. Photochem. Photobiol., A*, 2003, **154**, 235–243.
97 M. E. Alberto, N. Russo and C. Adamo, *Chem.–Eur. J.*, 2016, **22**, 9162–9168.
98 M. E. Alberto, C. Iuga, A. D. Quartarolo and N. Russo, *J. Chem. Inf. Model.*, 2013, **53**, 2334–2340.
99 B. J. Pankuch, D. E. Lacky and G. A. Crosby, *J. Phys. Chem.*, 1980, **84**, 2061–2067.
100 S. Decurtins, F. Felix, J. Ferguson, H. U. Guedel and A. Ludi, *J. Am. Chem. Soc.*, 1980, **102**, 4102–4106.
101 V. Balzani and A. Juris, *Coord. Chem. Rev.*, 2001, **211**, 97–115.
102 R. C. Young, T. J. Meyer and D. G. Whitten, *J. Am. Chem. Soc.*, 1976, **98**, 286–287.
103 M. B. Majewski, N. R. de Tacconi, F. M. MacDonnell and M. O. Wolf, *Inorg. Chem.*, 2011, **50**, 9939–9941.
104 B. Maubert, N. D. McClenaghan, M. T. Indelli and S. Campagna, *J. Phys. Chem. A*, 2003, **107**, 447–455.
105 N. D. McClenaghan, Y. Leydet, B. Maubert, M. T. Indelli and S. Campagna, *Coord. Chem. Rev.*, 2005, **249**, 1336–1350.
106 R. Wenger, V. Kurtcuoglu, C. Scholz, H. Marti and D. Hoogewijs, *Hypoxia*, 2015, 35.
107 L. K. McKenzie, H. E. Bryant and J. A. Weinstein, *Coord. Chem. Rev.*, 2019, **379**, 2–29.
108 K. G. Chen, R. D. Leapman, G. Zhang, B. Lai, J. C. Valencia, C. O. Cardarelli, W. D. Vieira, V. J. Hearing and M. M. Gottesman, *J. Natl. Cancer Inst.*, 2009, **101**, 1259–1271.
109 K. V. Sharma and L. M. Davids, *Photodiagn. Photodyn. Ther.*, 2012, **9**, 156–163.
110 A. Sparsa, S. Bellaton, T. Naves, M.-O. Jauberteau, J.-M. Bonnetblanc, V. Sol, M. Verdier and M.-H. Ratinaud, *Oncol. Rep.*, 2013, **29**, 1196–1200.